Fully Coupled Thermomechanical Analysis of Laminated Composites by Using Ordinary State Based Peridynamic Theory

Yan Gao and Selda Oterkus*

Department of Naval Architecture, Ocean and Marine Engineering, University of Strathclyde, Glasgow, G4 0LZ, United Kingdom

Abstract:

This study presents fully coupled ordinary state based peridynamic (PD) model for of laminated composites. The formulation includes coupling of both thermal and mechanical fields. In order to verify the proposed model, numerical simulations for benchmark problems are carried out and their results are compared with the ones from ANSYS solutions. First, the thermomechanical behaviour of the laminated composites subjected to both uniform and linear temperature changes are tested for single and multi-layer composites. Then, fully coupled thermo-mechanical formulations are validated for laminated composites subjected to pressure shock. Finally, the crack propagation paths and temperature distributions are predicted for shock loading conditions. In conclusion, the present PD model is well suited for solving fully coupled thermomechanical problems for laminated composites including crack initiations and propagations.

Keywords: Ordinary state based peridynamics, composites, fully coupled, thermomechanics, crack propagation

1 Introduction

In recent years, high performance composite materials like fibre-reinforced composites (FRCs) and carbon-carbon composites (CCCs) are increasingly used in aerospace and mechanical industries, especially for the working environments with mechanical shocks and large temperature variations [1]. The analyses of this type of problems have been carried out in the past using the uncoupled or semi-coupled thermoelasticity theory. It is assumed that the deformation induces relatively small temperature changes, and hence can be conveniently neglected. Only the effect of the temperature on the deformation field is considered. However, the coupling coefficient of composites is much larger than the metal materials. Furthermore, the coupling effect on temperature is significant under the loading conditions like a sudden change of temperature or a mechanical shock. Therefore, the deformation effect on temperature field is crucial in these cases. The uncoupled or semi-coupled analysis may not be accurate enough, and the employment of the fully coupled thermoelasticity theory is necessary in these cases [2].

*Corresponding Author: Selda Oterkus, Department of Naval Architecture, Ocean and Marine Engineering, University of Strathclyde. Email: selda.oterkus@strath.ac.uk

Many research achievements in the realm of fully coupled thermoelasticity are presented in the literature. Biot [3] introduced a modified Fourier heat transfer equation, predicting that the temperature cannot be calculated independently from deformation. In years of development, the theory of fully coupled thermoelasticity is well established, and some classical solutions to some basic problems are provided [4]. Dillon and Tauchert [5] experimentally investigated the heat generation during a small deformation, validating the coupling effect of deformation on the thermal field. Zenkour [6] compared the results of thermoelastic plate analyses by using three different theories, including the theory of coupled thermoelasticity. As to the composite materials, this problem becomes more complex because of the anisotropic property of composite materials. Stanley [7] presented an experiment to test the thermoelastic constants of composite materials under a compressive loading. Basic equations of linear thermoelasticity of a composite material were established in Ene's work [8]. Besides, a simple form of coupling constant was introduced to estimate the coupling effect for composite materials. In addition to the analytical and experimental methods, numerical methods are also popular in this field. Rao and Sinha [9] dealt with the coupled thermomechanical analysis of composites beams using finite element method (FEM), presenting different results from uncoupled analyses. Moreover, the coupled thermoelastic response of a composite plate subjected to thermal shock was studied by Mukherjee and Sinha [10] using FEM. Khan et al. [11] compared the temperature profiles from different FE models in the thermomechanical analysis of composites. Comparatively, boundary element method (BEM) was adopted by Kögl and Gaul [12] to investigate the coupling effect of composites. They stated that when linear elements were used, the BEM had an improved accuracy than FEM. Fully coupled thermomechanical analyses of one layer or equivalent single layer plate were given by Brischetto and Carrera [13], providing a wise approach for multi-layered composites.

In addition to thermoelasticity, failure analysis is also a hot topic in composite research. There are several kinds of failure exist in laminated composites materials, e.g. fibre/matrix debonding damage, fibre breakage, and interlaminar delamination. Although many mathematical models and computational methods have been developed to predict these failure mechanisms, high challenge still exist because of the adoption of continuum damage mechanics. Being different from the aforementioned numerical methods, i.e. BEM and FEM, peridynamic (PD) theory is a new numerical method based on non-local continuum theory. It was introduced by Silling [14] in an attempt to deal with the discontinues. In classical continuum mechanics (CCM), the equation of motion is a partial differential equation, resulting in singular stresses at crack tips. On the contrary, in PD theory, the equation of motion involves an integral form and thus holds everywhere in the body regardless of the presence of discontinues. Therefore, the PD theory is suitable for simulating cracks both for isotropic and composite materials. Oterkus and Madenci [15-17] successfully applied the bond based PD theory for composite materials. Kilic et al. [18] predicted the crack propagation in centre-cracked composites laminates using a bond based PD theory. Although bond based PD theory has been successfully employed in analysing composite materials, the material property is limited to having a fixed Poisson's ratio [14]. Additionally,

the major shear stiffness G_{12} of a lamina is also forced to be a fixed value related to the elastic modulus in fibre direction and transverse direction [19]. Consequently, if bond based peridynamic theory is utilized in analysing fibre reinforced composite lamina, four independent material constants $\left(E_1, E_2, G_{12}, \nu_{12}\right)$ will reduce to two independent constants $\left(E_1, E_2\right)$ [19]. On the other hand, state based peridynamic theory [20] which eliminates these limitations. Although various formulations are available for state based PD composites modelling, most of them are limited to mechanical analysis. Oterkus and Madenci [21] provided a fully coupled analysis of a fibre-reinforced lamina. And then the model was extended to multi-layer laminates by Gao and Oterkus [22]. But the bond based peridynamic theory is used for both models. To the authors' knowledge, fully coupled formulas and analyses for laminates are currently not available in ordinary state based peridynamic framework.

To address this concern, the focus of this paper is on fully coupled analysis of composite materials with ordinary state based peridynamic theory. Oterkus et al. [23] derived the heat conduction equation with ordinary state based peridynamic theory. Moreover, fully coupled thermomechanical equations for isotopic materials were proposed by Oterkus et al. [24] using bond based peridynamic theory and extended to ordinary state-based peridynamic form by Gao and Oterkus [25]. Based on their work, in this study both thermal and deformation fields are derived using ordinary state based peridynamic theory. The directional dependency of composite material properties, as well as the coupling effect on temperature is taken into account. Then the fully coupled thermomechanical numerical simulations are presented. A uniform and a linear temperature change are separately applied to both single layer and multi-layer composite models. The quasi-static mechanical deformations due to given temperature changes are compared against ANSYS solutions. Note that PD results should capture FEM solutions for the cases without damage. Moreover, PD is generally computationally more expansive with respect to FEM due to integral representation of its equation of motion. Next, pure heat conduction analyses of the multi-layer composite model are implemented to verify the thermal model. Further, pressure shock loads are applied to both single and multi-layer composite models for fully coupled thermomechanical analyses. Corresponding temperature and displacement profiles are compared with ANSYS in order to validate the proposed fully coupled thermomechanical formulations. Finally, failure analyses of single layer and multi-layer composite models with central pre-existing cracks are conducted by using fully coupled thermomechanical formulations. The progressive evolutions of cracking and temperature distributions are predicted.

2 Peridynamics Thermomechanics

The equations in peridynamic theory omit the partial derivatives of the deformation with respect to the spatial coordinates. Instead, integral-differential equations are adopted [14, 20, 26]. As illustrated in Fig. 1, in a body region R, each material point, $\mathbf{x}$, interacts only with all other points within its neighbourhood, $H_{\mathbf{x}}$. The maximum interaction distance denoted by δ is called the horizon. Also, $\mathbf{t}$

and $\mathbf{t}'$ are the force density vector, acting at material point $\mathbf{x}$ and $\mathbf{x}'$, respectively. In bond based PD theory, the force density vectors, $\mathbf{t}$ and $\mathbf{t}'$, are equal in magnitude and also parallel to their relative position in the deformed state. On the other hand, in ordinary state peridynamics, force density vectors $\mathbf{t}$ and $\mathbf{t}'$ are still parallel to the relative position, but they are not forced to be equal in magnitude. Thus, the ordinary state based peridynamic model overcomes the limitations of fixed Poisson's ratio as in case of bond based peridynamic model.

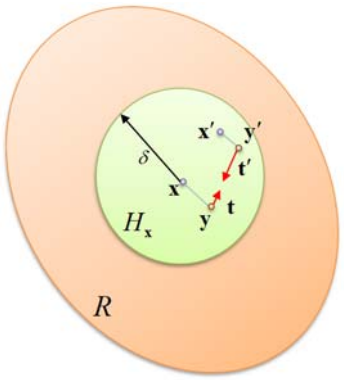

Fig. 1. Neighbourhood H_x centred at material point $\mathbf{x}$ in body region R.

The kinematics of PD material points is illustrated in Fig. 2. The material point k is the central point and material point j is one of its family members. The coordinates of the point k in the undeform and deformed configurations are $\mathbf{x}_k$ and $\mathbf{y}_k$, respectively. The corresponding displacement is denoted by $\mathbf{u}_k$. The bold symbols are used to represent vectors. The same notation is applied to other material point, e.g. j. With respected to the positive x direction, the bond angle is denoted by φ. The initial relative position and relative displacement vectors are defined as $\boldsymbol{\xi} = \mathbf{x}_j - \mathbf{x}_k$ and $\boldsymbol{\eta} = \mathbf{u}_j - \mathbf{u}_k$. Then the relative position in deformed configuration is $\mathbf{y}_j - \mathbf{y}_k = \boldsymbol{\xi} + \boldsymbol{\eta}$.

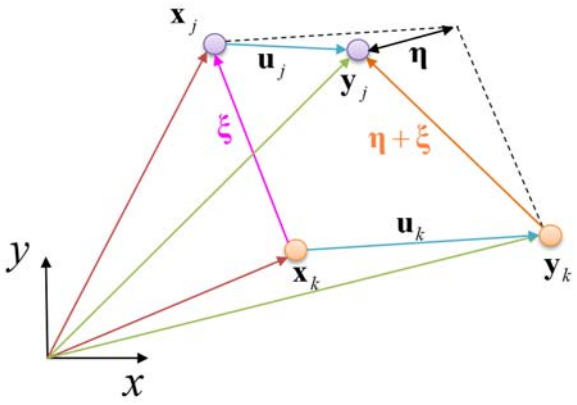

Fig. 2. Kinematics of PD material point k

Regarding the fully coupled thermomechanical problems, the PD formulations are derived based on irreversible thermodynamics, i.e. the conservation of energy and the free energy density function. The general form of the fully coupled thermomechanical equations based on state based peridynamic theory are given in [21, 24, 27-29] as

$$\rho\ddot{\mathbf{u}}\left(\mathbf{x}_k,t\right)=\sum_{j=1}^{N_{total}}\left(\mathbf{t}\left(\mathbf{u}_j-\mathbf{u}_k,\mathbf{x}_j-\mathbf{x}_k,t\right)-\mathbf{t}'\left(\mathbf{u}_k-\mathbf{u}_j,\mathbf{x}_k-\mathbf{x}_j,t\right)\right)V_j+\mathbf{b}\left(\mathbf{x}_k,t\right) \tag{1a}$$

$$\rho c_v\dot{T}\left(\mathbf{x}_k,t\right)=\sum_{j=1}^{N_{total}}\left(\kappa_{PD}\frac{\Theta\left(\mathbf{x}_j,t\right)-\Theta\left(\mathbf{x}_k,t\right)}{\left|\mathbf{x}_j-\mathbf{x}_k\right|}-\Theta_0\beta_{PD}\left(\mathbf{x}_j-\mathbf{x}_k\right)\dot{e}\left(\mathbf{x}_j-\mathbf{x}_k\right)\right)V_j+\rho q_b\left(\mathbf{x}_k,t\right) \tag{1b}$$

Eq.(1a) represents the PD form of the equation of motion. Thereby, ρ is the mass density and $\ddot{\mathbf{u}}\left(\mathbf{x}_k,t\right)$ is the acceleration of material point k at time t. In addition, N_{total} is the total number of family members of point *k*. Also, V_j is the volume of point j. The term $\mathbf{b}\left(\mathbf{x}_k,t\right)$ is the body force density at point k. The integration on the right-hand side of this equation represents the total peridynamic force acting on point k. Thereby, $\mathbf{t}\left(\mathbf{u}_j-\mathbf{u}_k,\mathbf{x}_j-\mathbf{x}_k,t\right)$ is used to represent the PD force density vector that point j exerts on point k. Similarly, $\mathbf{t}\left(\mathbf{u}_k-\mathbf{u}_j,\mathbf{x}_k-\mathbf{x}_j,t\right)$ represents the PD force density vector from point k to point j.

Eq.(1b) is the PD form of the equation of heat conduction including the deformation effect on thermal field. The specific heat capacity under constant volume is represented by c_v. In this equation, Θ_0 is the reference temperature and T is the temperature change with respect to reference temperature, $T=\Theta-\Theta_0$. Therefore, $\dot{T}\left(\mathbf{x}_k,t\right)$ represents the time rate of temperature change of point k at time t. The term $q_b\left(\mathbf{x}_k,t\right)$ is the prescribed volumetric heat generation per unit mass, κ_{PD} is the thermal micro conductivity [23]. The term $\Theta_0\beta_{PD}\left(\mathbf{x}_j-\mathbf{x}_k\right)\dot{e}\left(\mathbf{x}_j-\mathbf{x}_k\right)$ represents the effect of deformation on temperature. The term $\beta_{PD}\left(\mathbf{x}_j-\mathbf{x}_k\right)$ is the PD thermal modulus associated with the bond between point k and point j. Peridynamic thermal modulus and bond constants for 1-D, 2-D and 3-D bond based PD theory are given in [24, 28, 29]. Furthermore, $\dot{e}\left(\mathbf{x}_j-\mathbf{x}_k\right)$ is the time rate of change of bond extension, and it is defined as [21, 24, 27-29]

$$\dot{e}\left(\mathbf{x}_j-\mathbf{x}_k\right)=\frac{\mathbf{y}_j-\mathbf{y}_k}{\left|\mathbf{y}_j-\mathbf{y}_k\right|}\cdot\left(\dot{\mathbf{u}}_j-\dot{\mathbf{u}}_k\right) \tag{2}$$

3 Peridynamics Thermomechanics for Composite Materials

In the above section, the fully coupled thermomechanical PD theory is briefly reviewed. However, the fully coupled thermomechanical composite model in ordinary state based PD framework has not been established so far. The following section represents the derivation of fully coupled

thermomechanical formulations for ordinary state based peridynamics for composites by taking into account their directional properties.

3.1 Single layer PD composite model

In this section, fully coupled ordinary state based peridynamic single layer composite (lamina) model is developed in which the orthotropic property of lamina is taken into consideration. As shown in Fig. 3, it is presumed that the PD bonds are divided into three types according to their bond directions: fibre direction denoted by F, transverse direction denoted by T, and arbitrary direction denoted by FT [19, 30, 31]. Besides, the fibre angle is denoted by Φ.

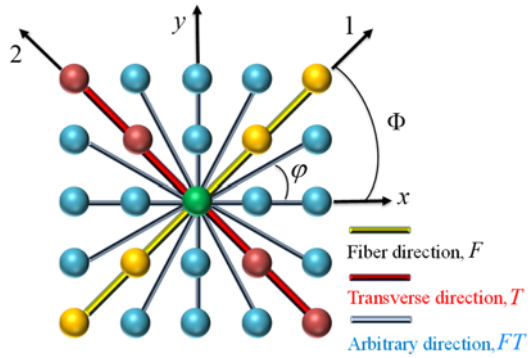

Fig. 3. Interaction of a family of material points for a fibre-reinforced lamina.

PD force density function provided in [30, 32] is modified by including the thermal effects as;

$$\mathbf{t}\left(\mathbf{u}_j-\mathbf{u}_k,\mathbf{x}_j-\mathbf{x}_k,t\right)=2\delta\left[\frac{d\Lambda_{kj}}{\left|\mathbf{x}_j-\mathbf{x}_k\right|}a\left(\theta_k-\left(\alpha_1+\alpha_2\right)T_k\right)+\left(\mu_F b_F\left(\mathbf{x}_k\right)+\mu_T b_T\left(\mathbf{x}_k\right)+b_{FT}\right)\left(s_{kj}-\alpha_\varphi T_k\right)\right]\frac{\mathbf{y}_j-\mathbf{y}_k}{\left|\mathbf{y}_j-\mathbf{y}_k\right|} \tag{3a}$$

and

$$\mathbf{t}\left(\mathbf{u}_k-\mathbf{u}_j,\mathbf{x}_k-\mathbf{x}_j,t\right)=-2\delta\left[\frac{d\Lambda_{kj}}{\left|\mathbf{x}_j-\mathbf{x}_k\right|}a\left(\theta_j-\left(\alpha_1+\alpha_2\right)T_j\right)+\left(\mu_F b_F\left(\mathbf{x}_j\right)+\mu_T b_T\left(\mathbf{x}_j\right)+b_{FT}\right)\left(s_{jk}-\alpha_\varphi T_j\right)\right]\frac{\mathbf{y}_j-\mathbf{y}_k}{\left|\mathbf{y}_j-\mathbf{y}_k\right|} \tag{3b}$$

where

$$\mu_F=\begin{cases}1 & \left(\mathbf{x}_j-\mathbf{x}_k\right)\text{// fibre direction}\\ 0 & \text{otherwise}\end{cases} \tag{4a}$$

with

$$\mu_T=\begin{cases}1 & \left(\mathbf{x}_j-\mathbf{x}_k\right)\perp\text{ fibre direction}\\ 0 & \text{otherwise}\end{cases} \tag{4b}$$

In Eq. (3) T_k and T_j are the temperature changes of point k and j with respect to reference temperature Θ_0. Besides, α_1 and α_2 represent the thermal expansion coefficients in fibre and transverse direction, respectively. Thereby, α_φ represents the thermal expansion coefficient at any direction as [15]

$$\alpha_\varphi = \alpha_x \cos^2(\varphi) + \alpha_y \sin^2(\varphi) + \alpha_{xy} \sin(\varphi)\cos(\varphi) \tag{5}$$

with [33]

$$\alpha_x = \alpha_1 \cos^2(\Phi) + \alpha_2 \sin^2(\Phi) \tag{6a}$$

$$\alpha_y = \alpha_1 \sin^2(\Phi) + \alpha_2 \cos^2(\Phi) \tag{6b}$$

In Eq. (3) θ_k and θ_j are the dilatations of point k and j, respectively [19, 30]. The dilatation for a single layer PD model is also modified by including the thermal effects as

$$\theta_k = d\delta \sum_{j=1}^{N_{ply}} \left(s_{kj} - \alpha_\varphi T_k\right) \Lambda_{kj} V_j + \left(\alpha_1 + \alpha_2\right) T_k \tag{7}$$

with $d = \dfrac{2}{\pi h \delta^3}$ and N_{ply} represents the total number of the family members within the same layer.

In Eq. (3) and (7) s_{kj} is the bond stretch. It is defined as [19, 30]

$$s_{kj} = \frac{\left|\mathbf{y}_j - \mathbf{y}_k\right| - \left|\mathbf{x}_j - \mathbf{x}_k\right|}{\left|\mathbf{x}_j - \mathbf{x}_k\right|} \tag{8}$$

The PD auxiliary parameter Λ_{kj} is defined as [30]

$$\Lambda_{kj} = \left(\frac{\mathbf{y}_j - \mathbf{y}_k}{\left|\mathbf{y}_j - \mathbf{y}_k\right|}\right) \cdot \left(\frac{\mathbf{x}_j - \mathbf{x}_k}{\left|\mathbf{x}_j - \mathbf{x}_k\right|}\right) \tag{9}$$

In Eq.(3) , the peridynamic parameters b_F , b_T and b_{FT} are associated with deformation of collective points in the fibre, transverse and other directions, respectively. The peridynamic parameters in Eq. (3) are defined as [30]:

$$a = \frac{1}{2}\left(Q_{12} - Q_{66}\right) \tag{10a}$$

$$b_{FT} = \frac{6Q_{66}}{\pi h \delta^4} \tag{10b}$$

$$b_F = \frac{\left(Q_{11} - Q_{12} - 2Q_{66}\right)}{2\delta \sum_{j=1}^{N_f} \left|\mathbf{x}_j - \mathbf{x}_k\right| V_j} \tag{10c}$$

$$b_T = \frac{\left(Q_{22} - Q_{12} - 2Q_{66}\right)}{2\delta \sum_{j=1}^{N_t} \left|\mathbf{x}_j - \mathbf{x}_k\right| V_j} \tag{10d}$$

where N_f, N_t are the total number of bonds in the fibre and transverse direction respectively (Fig. 3) and $[Q]$ is the reduced stiffness matrix. The reduced stiffness matrix is defined as [34]

$$[Q] = \begin{bmatrix} Q_{11} & Q_{12} & 0 \\ Q_{21} & Q_{22} & 0 \\ 0 & 0 & Q_{66} \end{bmatrix} \tag{11a}$$

with

$$Q_{11} = \frac{E_1}{1 - \nu_{12}\nu_{21}}, Q_{22} = \frac{E_2}{1 - \nu_{12}\nu_{21}}, Q_{12} = \frac{\nu_{12}E_2}{1 - \nu_{12}\nu_{21}}, Q_{66} = G_{12} \tag{11b}$$

In Eq. (11b), E_1, E_2, G_{12}, ν_{12} and ν_{21} represent the elastic modulus in fibre direction, the elastic modulus in transverse direction, major shear modulus, major Poisson's ratio and minor Poisson's ratio, respectively.

Similarly, the directional dependency properties are also taken into consideration in the heat equation given in Eq.(1b). Therefore, thermal micro conductivity proposed by Oterkus and Madenci [21] for a lamina is adopted as

$$\kappa_{PD} = \begin{cases} \kappa_f + \kappa_m & \text{for fibre direction} \\ \kappa_m & \text{otherwise.} \end{cases} \tag{12}$$

where κ_m and κ_f represent the peridynamic micro conductivities for fibre and other directions as [21]

$$\kappa_m = \frac{6k_2}{\pi h \delta^3} \tag{13a}$$

and

$$\kappa_f\left(\mathbf{x}_k\right) = \frac{2\left(k_1 - k_2\right)}{\sum_{j=1}^{N_f} \left|\boldsymbol{\xi}\right| V_j} \tag{13b}$$

In Eq. (13), k_1 and k_2 represent the thermal conductivities in CCM for fibre and transverse direction. PD thermal moduli in fibre and other directions are defined as (Appendix B)

$$\beta_{PD} = \begin{cases} \beta_f + \beta_m & \text{for fibre direction} \\ \beta_m & \text{otherwise.} \end{cases} \tag{14}$$

with

$$\beta_m = \frac{3\left(Q_{12}\alpha_1 + Q_{22}\alpha_2\right)}{\pi h \delta^3} \tag{15a}$$

and

$$\beta_f(\mathbf{x}_k)=\frac{(Q_{11}\alpha_1+Q_{12}\alpha_2)-(Q_{12}\alpha_1+Q_{22}\alpha_2)}{\sum_{j=1}^{N_f}|\boldsymbol{\xi}|V_j} \tag{15b}$$

As a summary, the ordinary state based PD formulation for a single layer is given as;

$$\begin{aligned}\rho\ddot{\mathbf{u}}(\mathbf{x}_k,t)=\sum_{j=1}^{N_{ply}}2\delta\Bigg[&\frac{d\Lambda_{kj}}{|\mathbf{x}_j-\mathbf{x}_k|}a\left(\theta_k+\theta_j-(\alpha_1+\alpha_2)(T_k+T_j)\right)\\&\left(\mu_F b_F(\mathbf{x}_k)+\mu_T b_T(\mathbf{x}_k)+b_{FT}\right)\left(s_{kj}-\alpha_\varphi T_k\right)\\&\left(\mu_F b_F(\mathbf{x}_j)+\mu_T b_T(\mathbf{x}_j)+b_{FT}\right)\left(s_{jk}-\alpha_\varphi T_j\right)\Bigg]\frac{\mathbf{y}_j-\mathbf{y}_k}{|\mathbf{y}_j-\mathbf{y}_k|}V_j+\mathbf{b}(\mathbf{x}_k,t)\end{aligned} \tag{16a}$$

$$\rho c_v\dot{T}(\mathbf{x}_k,t)=\sum_{j=1}^{N_{ply}}\left[\left(\mu_F\kappa_f+\kappa_m\right)\frac{\Theta_j-\Theta_k}{|\boldsymbol{\xi}_{kj}|}-\Theta_0\left(\mu_F\beta_F+\beta_m\right)\dot{e}_{kj}\right]V_j+\rho q_b(\mathbf{x}_k,t) \tag{16b}$$

Here Θ_j and Θ_k represent the temperatures at point j and k, respectively.

3.2 Multi-layer PD composite model

The single layer PD models can be assembled into multi-layer models (laminate) with arbitrary stacking sequences. Additional bonds, also called interlayer bonds, are added to connect points between neighbouring plies. According to [30], shown in Fig. 4, the peridynamic bonds in multi-layer model fall into three categories: in-plane bonds, transverse normal bonds, transverse shear bonds. The in-plane bonds have already been discussed in the single layer model, so only the latter two bonds belonging to interlayer bonds will be explained in this section.

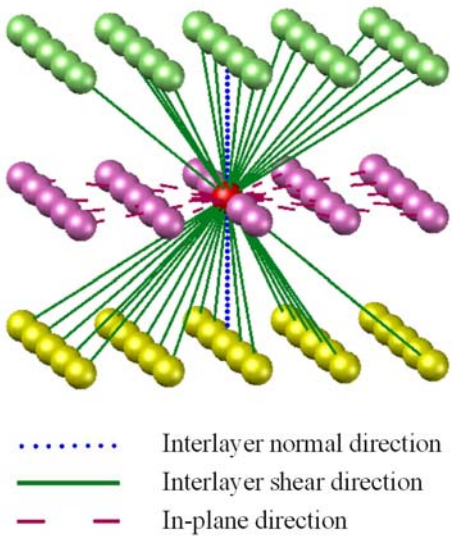

Fig. 4. Classification of PD bonds in multi-layer composites model.

As illustrated in Fig. 5, the equation of motion for material point k in n^{th} ply can be expressed as [30]

$$\rho_k^n \ddot{\mathbf{u}}_k^n = \sum_{j=1}^{N_{ply}} \left(\mathbf{t}_{kj}^n - \mathbf{t}_{jk}^n \right) V_j^n + \sum_{m=n+1,n-1} \mathbf{P}_k^{nm} V_k^m + 2 \sum_{m=n+1,n-1} \sum_{j=1}^{N_{shear}} \mathbf{q}_{kj}^{nm} V_j^m + \mathbf{b}_k^n \tag{17}$$

where $\mathbf{P}_k^{nm}$ represents the PD force density vector due to transverse normal bond and $\mathbf{q}_{kj}^{nm}$ is the force density vector associated with transverse shear deformation. The superscripts, n and m, represent the sequence number of layer where the material point is located. The term N_{shear} represents the number of family members connecting to $\mathbf{x}_k$ through interlayer shear bonds. It should be noted that the first term on the right hand side of Eq. (17) is presented in section 3.1.

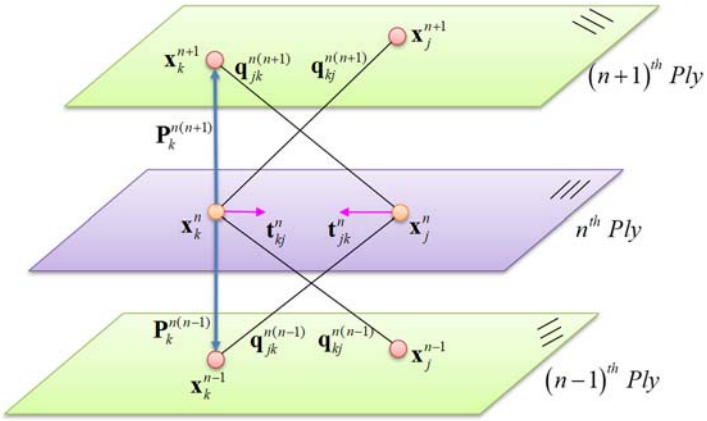

Fig. 5. Representation of interactions of material point k in multi-layer composite model.

In the transverse normal deformation, the laminate (resin-rich layer) is treated as the matrix material in its thickness direction [30]. Therefore, the material properties in thickness direction are assumed same as the material properties of matrix, i.e.

$$E_z = E_m, G_z = G_m \text{ and } \alpha_z = \alpha_m \tag{18}$$

where the subscript m represents the matrix material. The transverse normal force density function including the thermal effects is represented as

$$\mathbf{P}_k^{nm} = 4 b_N \hat{\delta} \left(s_k^{nm} - \alpha_m T_{avg,k}^{nm} \right) \frac{\mathbf{y}_k^m - \mathbf{y}_k^n}{\left| \mathbf{y}_k^m - \mathbf{y}_k^n \right|} \tag{19}$$

where $\mathbf{P}_k^{nm}$ represents the force density between point k in n^{th} ply and its corresponding point in m^{th} ply with the same in-plane coordinate. The term $\hat{\delta}$ is the horizon in transverse normal direction. The term $T_{avg,k}^{nm}$ is the average temperature change of point $\mathbf{x}_k^n$ and $\mathbf{x}_k^m$. The transverse normal peridynamic parameter, b_N, is given as [30];

$$b_N = \frac{E_m}{\hat{\delta} \left[\left(h_{n+1} + h_n \right) V_k^{n+1} + \left(h_{n-1} + h_n \right) V_k^{n-1} \right]} \tag{20}$$

where h_{n+1}, h_n and h_{n-1} are illustrated in Fig. 6(a).

Similarly, transverse shear bond force density function can be modified by including the thermal effects as;

$$\mathbf{q}_{kj}^{nm} = 4b_s\tilde{\delta}\left(\left(s_{kj}^{nm} - \alpha_m T_{avg,kj}^{nm}\right) - \left(s_{jk}^{nm} - \alpha_m T_{avg,jk}^{nm}\right)\right)\frac{\mathbf{y}_j^m - \mathbf{y}_k^n}{\left|\mathbf{y}_j^m - \mathbf{y}_k^n\right|} \tag{21a}$$

or

$$\mathbf{q}_{kj}^{nm} = 4b_s\tilde{\delta}\frac{\phi_{kj}^{nm}\left(h_m + h_n\right)}{\left|\mathbf{x}_j^m - \mathbf{x}_k^n\right|}\frac{\mathbf{y}_j^m - \mathbf{y}_k^n}{\left|\mathbf{y}_j^m - \mathbf{y}_k^n\right|} \tag{21b}$$

with

$$\phi_{kj}^{nm} = \left|\mathbf{x}_j^m - \mathbf{x}_k^n\right|\frac{\left(s_{kj}^{nm} - \alpha_m T_{avg,kj}^{nm}\right) - \left(s_{jk}^{nm} - \alpha_m T_{avg,jk}^{nm}\right)}{h_m + h_n} \tag{21c}$$

where h_m and h_n are the thickness of m^{th} and n^{th} layer in the laminate, respectively. Here m^{th} layer represents the one layer above or one layer below the n^{th} layer (Fig. 6 (a)). Thereby, ϕ_{kj}^{nm} represents the average shear angle in interlayer shear direction. The term $\mathbf{q}_{kj}^{nm}$ is the transverse shear force density vector between material point k in n^{th} ply and material point j in m^{th} ply. The horizon in transverse shear direction, $\tilde{\delta}$, is defined as $\tilde{\delta} = \sqrt{\delta^2 + \hat{\delta}^2}$ (Fig. 6(b)). The term b_S is a PD parameter and it is given as [30];

$$b_S = \frac{G_m}{8\pi\tilde{\delta}}\frac{1}{\left\{\begin{array}{l}\left(\frac{h_{n+1}+h_n}{2}\right)^3\left[\delta^2 + 2\left(\frac{h_{n+1}+h_n}{2}\right)^2 / \sqrt{\delta^2 + \left(\frac{h_{n+1}+h_n}{2}\right)^2} - \left(h_{n+1}+h_n\right)\right] \\ + \left(\frac{h_{n-1}+h_n}{2}\right)^3\left[\delta^2 + 2\left(\frac{h_{n-1}+h_n}{2}\right)^2 / \sqrt{\delta^2 + \left(\frac{h_{n-1}+h_n}{2}\right)^2} - \left(h_{n-1}+h_n\right)\right]\end{array}\right\}} \tag{22}$$

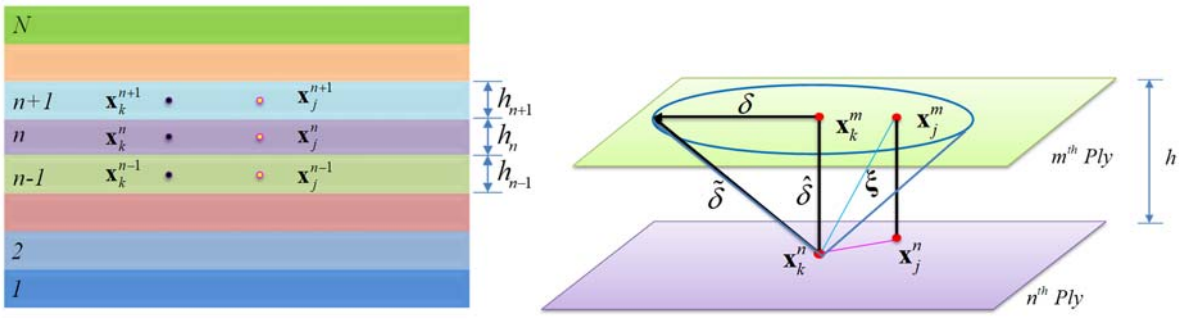

Fig. 6. (a) Illustration of each lamina in a laminate with N represent the total number of layers; (b) Horizon in transverse shear direction

Similarly, the effect of interlayer thermal bonds is considered in the coupled heat equation by modifying Eq. (16b) as

$$\rho c_v \dot{T}_k^n = \sum_{j=1}^{N_{ply}} \left[\left(\mu_F \kappa_f + \kappa_m \right) \frac{\Theta\left(\mathbf{x}_j^n, t\right) - \Theta\left(\mathbf{x}_k^n, t\right)}{\left|\mathbf{x}_j^n - \mathbf{x}_k^n\right|} - \Theta_0 \left(\mu_F \beta_f + \beta_m \right) \dot{e}_{kj}^n \right] V_j^n + \sum_{m=n+1,n-1} \sum_{j=1}^{N_{inter}} \left[\kappa_{inter} \frac{\Theta\left(\mathbf{x}_j^m, t\right) - \Theta\left(\mathbf{x}_k^n, t\right)}{\left|\mathbf{x}_j^m - \mathbf{x}_k^n\right|} - \Theta_0 \beta_{inter} \dot{e}_{kj,z}^{nm} \right] V_j^m + \rho q_b \left(\mathbf{x}_k^n, t\right) \tag{23}$$

The second term on the right hand side of Eq. (23) represents the heat flow between adjacent layers. N_{inter} is the family member number those connect to $\mathbf{x}_k^n$ through interlayer thermal bonds. Rate of change of bond extension is considered only through the thickness direction for interlayer thermal bonds. Interlayer PD micro conductivity and PD thermal modulus are given as (Appendix A and B)

$$\kappa_{inter} = \frac{k_m}{2\pi h^3 \left(\tilde{\delta} - h \right)} \tag{24}$$

and

$$\beta_{inter} = \frac{E_m \alpha_m}{4\pi h^3 \left(\tilde{\delta} - h \right)} \tag{25}$$

3.3 Failure criteria

The failure in peridynamic theory is simulated by breaking PD bonds irreversibly. When a PD bond is stretched beyond a critical value, the bond fails. The equation of motion in PD uses integrals, applying everywhere regardless of discontinuities. Therefore, damage is directly incorporated in the material response. The mode mixity effects can be captured by the selected failure criteria, which is demonstrated by Vazic et al. [35]. The PD predictions for failure mode ranging from pure mode I to pure model II are consistent with the experiments [36].

Because of the four different types of PD bonds in a multi-layer composites model, four different critical stretch values are needed in the failure analyses. The critical stretch values are considered as [30, 37]

$$s_m = \sqrt{\frac{G_{IC}}{\left(\frac{6}{\pi} \mu_m + \frac{16}{9\pi^2} \left(K_m - 2\mu_m \right) \right) \delta}} \tag{26a}$$

$$s_f = \frac{\sigma_{1t}}{E_1} \tag{26b}$$

$$s_{in} = \sqrt{\frac{2G_{IC}}{hE_m}} \tag{26c}$$

$$\phi_c = \sqrt{\frac{G_{IIC}}{hG_m}} \tag{26d}$$

where s_m, s_f, s_{in}, ϕ_c are the critical stretch values for matrix bonds, fibre bonds, interlayer normal bonds, and interlayer shear bonds, respectively. The material constants K_m and μ_m are bulk modulus and Lamé constant of matrix material. Besides, G_{IC} and G_{IIC} are critical energy release rate for the first and second failure mode in classical fracture mechanics, respectively. The term σ_{1t} is the tension strength property of a single ply. The critical stretch in Eq.26(b) has a similar meaning of critical strain in the context of classical continuum mechanics. On the other hand, the critical stretches given in Eqs. 26 (a,c,d) are obtained by equating the energies required to eliminate all PD interactions across the crack surfaces to the mode I or mode II critical energy release rates. Thus, the failure criteria mentioned in equations 26(a,c,d) are energy-based [30].

Eq. 26(a) and 26(b) are related with intralaminar failure mode. Eq. 26(a) corresponds to matrix damage and splitting failure mode. Eq. 26(b) corresponds to fibre damage. Eq.26(c) and 26(d) are related with interlaminar failure mode. Eq. 26(c) corresponds to interlaminar mode-I fracture and Eq. 26(d) corresponds to interlaminar mode-II fracture as shown in Fig. 7

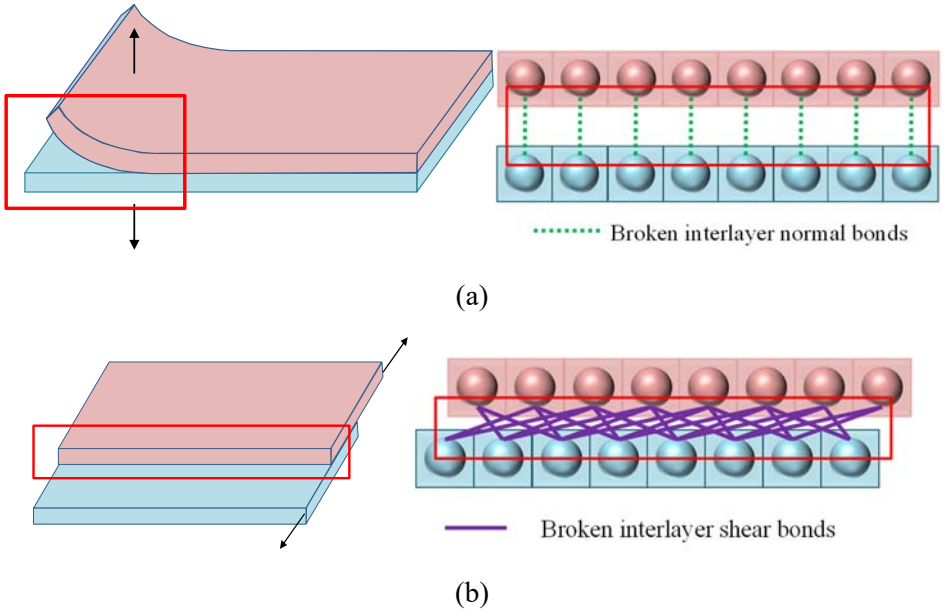

Fig. 7 Interlaminar failure modes: (a) Mode-I Fracture; (b) Mode-II Fracture

A history dependent failure function, χ, is defined for each interaction to indicate the bond breakage as [30, 37, 38]

$$\chi_{\text{fiber}}\left(\mathbf{x}_j-\mathbf{x}_k,\mathbf{y}_j-\mathbf{y}_k,t\right)=\begin{cases}1 \text{ for } \left(s_{kj}-\alpha_1 T_{avg,kj}\right)<s_f\\ 0 \text{ for } \left(s_{kj}-\alpha_1 T_{avg,kj}\right)\geq s_f\end{cases} \tag{27a}$$

$$\chi_{\text{matrix}}\left(\mathbf{x}_j-\mathbf{x}_k,\mathbf{y}_j-\mathbf{y}_k,t\right)=\begin{cases}1 \text{ for } \left(s_{kj}-\alpha_\varphi T_{avg,kj}\right)<s_m\\ 0 \text{ for } \left(s_{kj}-\alpha_\varphi T_{avg,kj}\right)\geq s_m\end{cases} \tag{27b}$$

$$\chi_{\text{inter,normal}}\left(\mathbf{x}_j-\mathbf{x}_k,\mathbf{y}_j-\mathbf{y}_k,t\right)=\begin{cases}1 \text{ for } \left(s_{kj}-\alpha_m T_{avg,kj}\right)<s_{in}\\ 0 \text{ for } \left(s_{kj}-\alpha_m T_{avg,kj}\right)\geq s_{in}\end{cases} \tag{27c}$$

$$\chi_{\text{inter,shear}}\left(\mathbf{x}_j-\mathbf{x}_k,\mathbf{y}_j-\mathbf{y}_k,t\right)=\begin{cases}1 \text{ for } \phi_{kj}^{nm}<\phi_c\\ 0 \text{ for } \phi_{kj}^{nm}\geq\phi_c\end{cases} \tag{27d}$$

where χ_{fibre}, χ_{matrix}, $\chi_{\text{inter,normal}}$ and $\chi_{\text{inter,shear}}$ are related with fibre bonds, matrix bonds, interlayer normal bonds, interlayer shear bonds. The damage level at a point is represented by local damage parameter as [39];

$$\varphi\left(\mathbf{x}_k,t\right)=1-\frac{\sum_{j=1}^{N_{total}}\chi\left(\mathbf{x}_j-\mathbf{x}_k,\mathbf{y}_j-\mathbf{y}_k,t\right)V_j}{\sum_{j=1}^{N_{total}}V_j} \tag{28}$$

4 Numerical simulations

In order to validate the derived ordinary state based thermomechanical PD formulations, several numerical simulations are conducted, and then the results are mainly compared with those obtained from ANSYS solutions. Firstly, in section 4.1, temperature changes are imposed to the composite models to estimate the equation of motion which includes the thermal loading. Secondly, heat transfer simulations in multi-layer composites are implemented in section 4.2, in order to validate the developed PD thermal model for multi-layer composites. Thirdly, pressure shock loads are applied in fully coupled thermomechanical analyses in sections 4.3. The emphasis is put on the predictions of the displacements and the temperature, which act as primary variables in the simulations. And the validity of the fully coupled thermomechanical PD model is investigated by the comparisons of the simulation results with ANSYS solution. Finally, in section 4.4, failure analyses with central pre-existing cracks on the models are carried out. The crack propagation paths and the temperature distribution evolutions are predicted.

During the numerical simulations, the composite material is chosen as graphite/epoxy. The material properties are listed in [34]. The length and width of the single layer composite model specified as $0.1\,\text{m}$. The thickness of the single layer model is $0.001\,\text{m}$. The multi-layer composite model is constructed with three single layer models with a ply stacking sequence of $[0/90/0]$, as illustrated in Fig. 7. Each ply is modelled as a two-dimensional orthotropic structure with one node in the thickness direction. The models are discretized into 200 subdomains both in x and y directions, leading to a space between material points, Δ, as $5\times10^{-4}\,\text{m}$. High accuracy and desired numerical efficiency can be achieved by adopting this grid size. The in-plane horizon is chosen as $\delta=3.015\Delta$, which is

recommended by [39] and [30]. The origin of the coordinate system is set at the middle of the bottom ply as illustrated in Fig. 7. The reference temperature is $\Theta_0 = 285$ K.

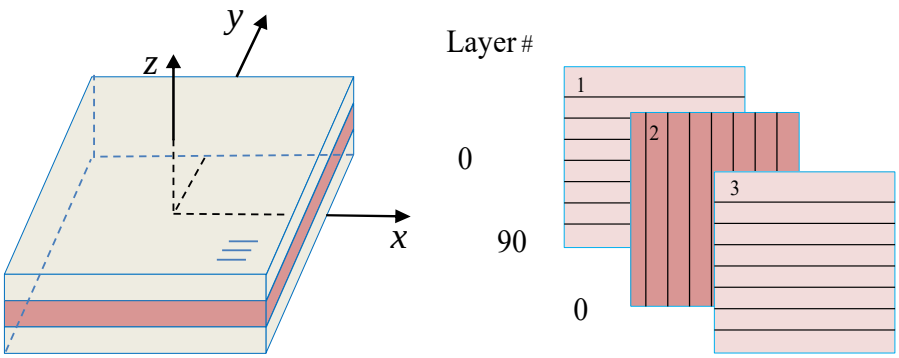

Fig. 7. Multi-layer composite model with stacking sequence $[0/90/0]$.

Table 1 Material property of composites [34]

Mechanical Properties		Thermal Properties	
Longitudinal elastic modulus E_1 (GPa)	181	Longitudinal coefficient of thermal expansion α_1 $(\mu\text{m/m/K})$	0.02
Transverse elastic modulus E_2 (GPa)	10.3	Transverse coefficient of thermal expansion α_2 $(\mu\text{m/m/K})$	22.5
Shear modulus G_{12} (GPa)	7.17	Longitudinal thermal conductivity k_1 (W/m/K)	8.3075
Major Poisson's ratio ν_{12}	0.28	Transverse thermal conductivity k_2 (W/m/K)	0.7575
Mass density ρ (kg/m^3)	1620	Specific heat c_v (J/kg/K)	1092.728
Elastic modulus of matrix material E_m (GPa)	3.4	Thermal conductivity of matrix material k_m (W/m/K)	0.2
Shear modulus of matrix material G_m (GPa)	1.308	Thermal expansion coefficient of matrix material α_m $(\mu\text{m/m/K})$	63

4.1 Composite subject to temperature change

In this section, temperature changes are imposed to both the single-layer and multi-layer composite models. All four edges of both composite models are free to deform and they are insulated. An adaptive dynamic relaxation (ADR) approach introduced by Kilic and Madenci [40] is utilized for the quasi-static analyses. A unit time step size is used to save the computational time [30]. The displacements predictions are compared with the ones from ANSYS or classical laminate theory (CLT) [41] solutions.

4.1.1 Constant temperature change

As a first case, simple loading condition, i.e. a constant temperature change of 50 K , is applied to single layer composite with a fibre orientation of $\Phi=0^{\circ}$ is considered. The analytical solution based on the CLT for a single layer ply can be calculated as [42];

$$u_x\left(x, y=0\right)=\alpha_1\left(\Delta T\right)x \tag{29a}$$

$$u_y\left(x=0, y\right)=\alpha_2\left(\Delta T\right)y \tag{29b}$$

The term u_x and u_y represent the horizontal and vertical components of displacement.

During the numerical simulations, convergence study is utilised by tracing the displacements of a point as shown in Fig. 8. The horizontal and vertical displacements predictions along the central lines of the single layer model are provided in Fig. 9. The good agreements indicate the successful application of the state based PD equation of motion by considering the effect of temperature on mechanical field.

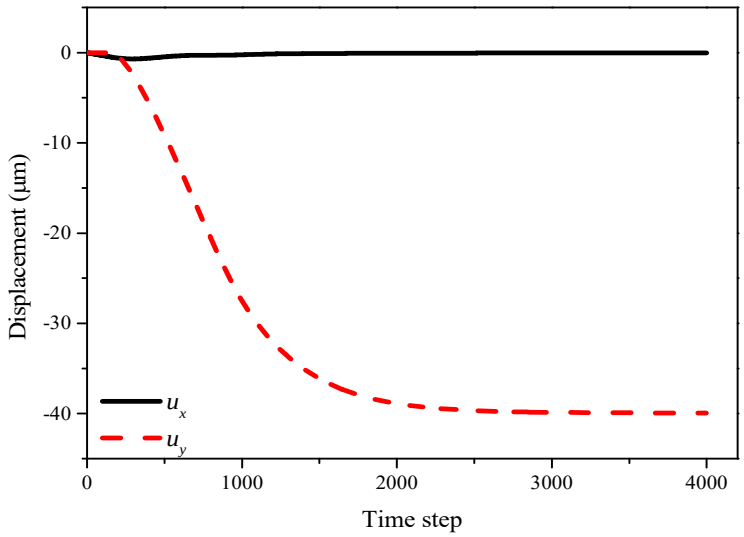

Fig. 8. Convergence study by tracing the displacements of the material point at $x=-0.0495\,\mathrm{m}$ and $y=-0.0355\,\mathrm{m}$.

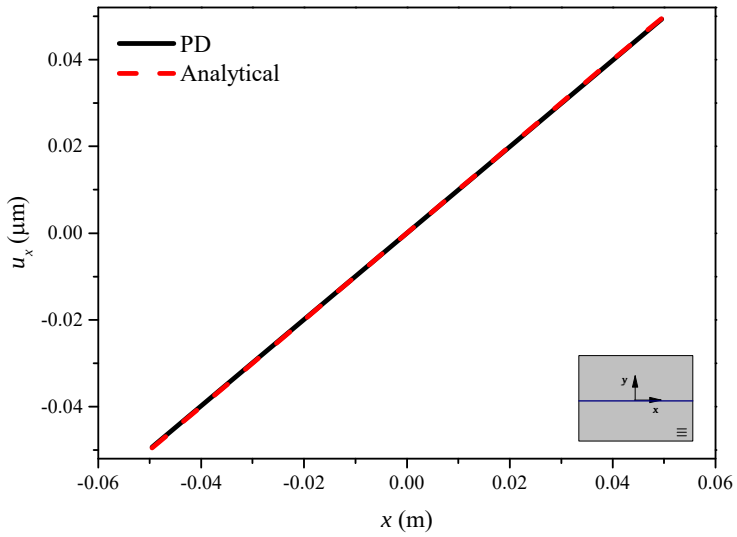

(a)

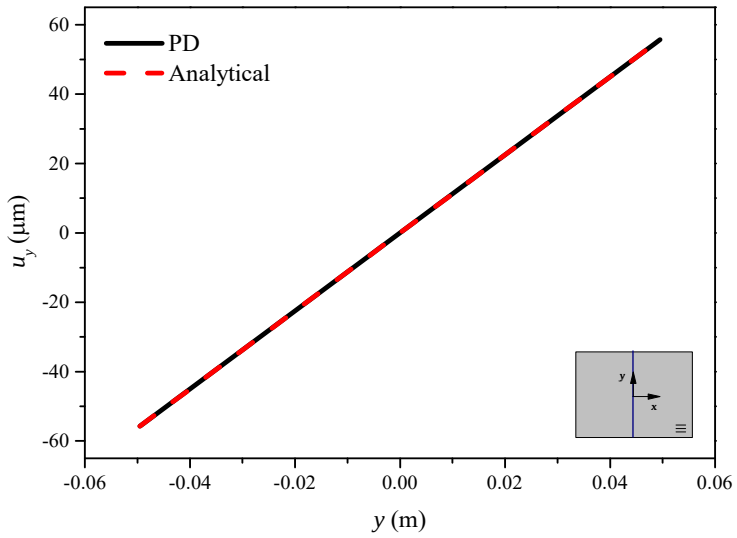

(b)

Fig. 9. (a) Horizontal (b) Vertical displacements along the central lines of the single layer model subjected to constant temperature change.

As a second case, the same constant temperature change is imposed to the multi-layer composite model. The analytical solution based on the CLT for multi-layer composite model can be calculated as [42];

$$u_x = \alpha_x^* (\Delta T) x \tag{30a}$$

$$u_y = \alpha_y^* (\Delta T) y \tag{30b}$$

$$u_z = \alpha_m (\Delta T) z \tag{30c}$$

where α_x^* and α_y^* are the thermal expansion coefficients of the laminate with respect to the global coordinate system. They can be presented as [42]

$$\{\alpha^*\} = [A]^{-1} \sum_{k=1}^{N} [\bar{Q}]^k \{\alpha\}_{xy}^k h_k \tag{31a}$$

with

$$\left\{\alpha^*\right\}=\left\{\alpha_x^*, \alpha_y^*, \alpha_{xy}^*\right\} \tag{31b}$$

and

$$[A]=\sum_{k=1}^{N}\left[\bar{Q}\right]^k h_k \tag{31c}$$

where $\left[\bar{Q}\right]^k$ is the reduced transformed stiffness matrix as defined in Eq. (11a), $\{\alpha\}_{xy}^k$ is the thermal expansion coefficient vector with respect to the global coordinate system and h_k is the thickness of the k^{th} layer. In ANSYS, the solid element type SOLID186 is utilized in the static analysis. The mesh size in x and y directions is 2×10^{-3} m with three elements in the z direction.

The displacement components along the midline of the multi-layer composite model obtained from PD , ANSYS and analytical simulations are compared and presented in Fig. 10. It can be easily observed that, the results from these methods agree very well. Thus, the PD equation of motion formulations for multi-layer composite under a constant temperature change is validated. There is a slight difference between PD results and classical ones near the boundary due to the PD surface effect [43]. It should be noted that the deformation of multi-layer composite differs significantly from the single layer because of the orientation of each ply in the stacking sequence.

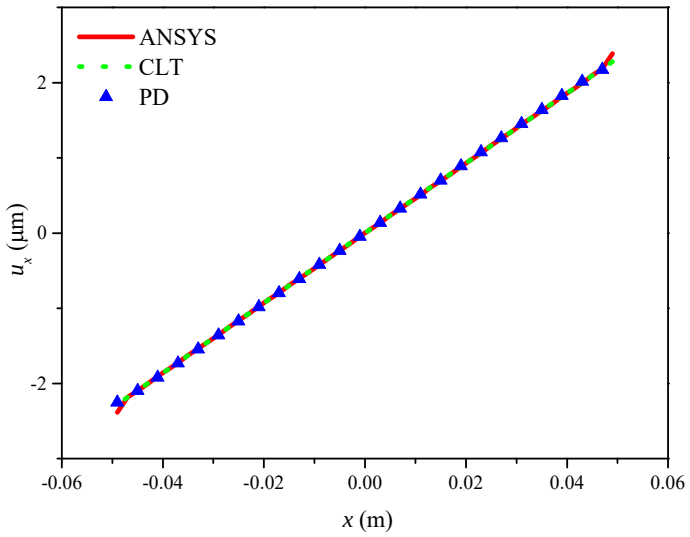
ANSYS
CLT
PD
u_x (μm)
2
0
-2
-0.06
-0.04
-0.02
0.00
0.02
0.04
0.06
x (m)

(a)

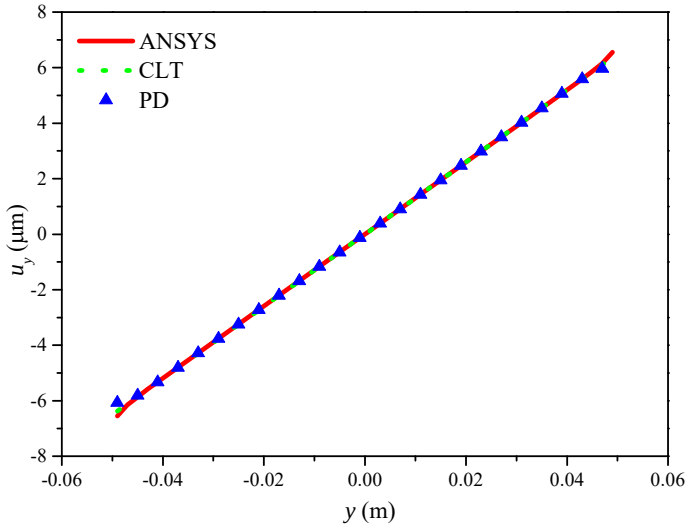
ANSYS
CLT
PD
u_y (μm)
8
6
4
2
0
-2
-4
-6
-8
-0.06
-0.04
-0.02
0.00
0.02
0.04
0.06
y (m)

(b)

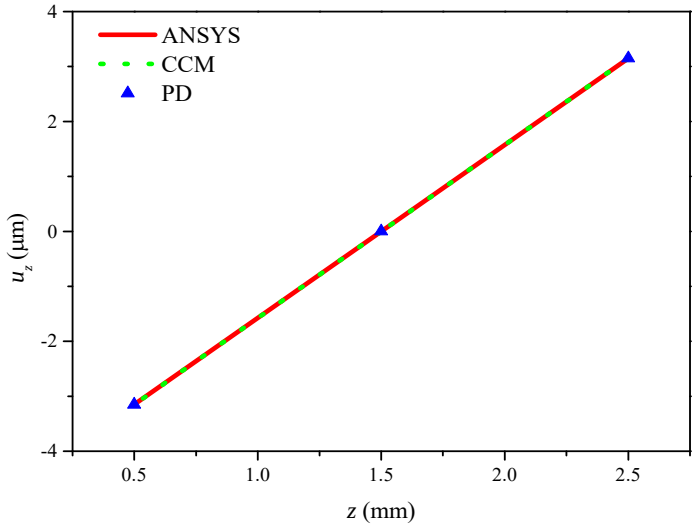
ANSYS
CCM
PD
u_z (μm)
4
2
0
-2
-4
0.5
1.0
1.5
2.0
2.5
z (mm)

(c)

Fig. 10. (a) Horizontal (b) Vertical (c) Out of plane displacements along the central lines of the multi-layer model subjected to constant temperature change.

4.1.2 Linear temperature change

The thermal loading is changed to a linear temperature change, $\Delta T = 500x\,(\mathrm{K})$ with x representing the horizontal location. As a first case, the non-uniform temperature change is applied for single layer composite model. In ANSYS, the plane element type PLANE182 with the plane stress assumption is utilized in the static analysis. The mesh size is 1×10^{-3} m with only one element in the thickness direction. As shown in Fig. 11 and 13, the horizontal and vertical displacements predictions from peridynamic solutions are in agreement with the ANSYS predictions.

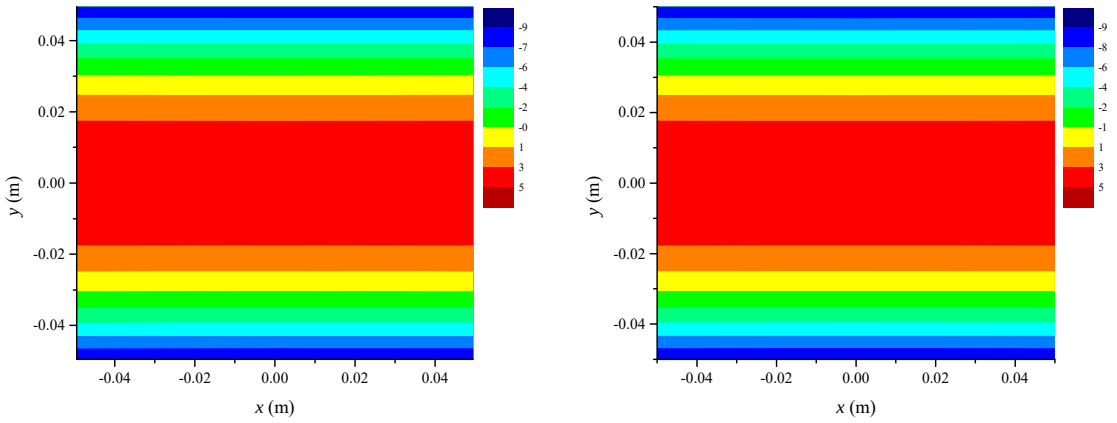

Fig. 11. Horizontal displacements, $u_x\,(\mu\mathrm{m})$ (a) PD and (b) ANSYS results

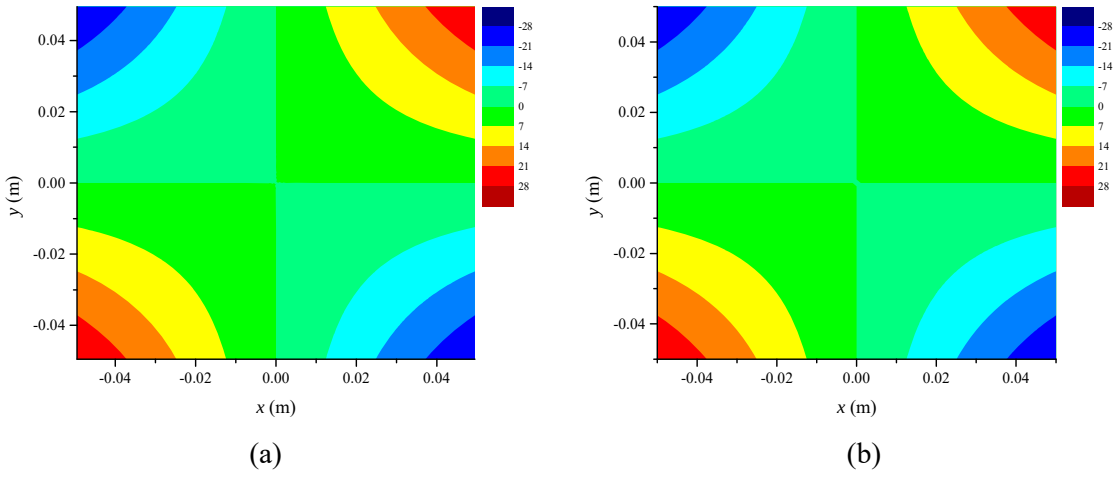

Fig. 12. Vertical displacements, $u_y\,(\mu\mathrm{m})$ (a) PD and (b) ANSYS results

As a second case, the same linear temperature change is applied to multi-layer composite model. The ANSYS model is same as described in section 4.1.1. The displacements components are compared with ANSYS predictions, as shown in Fig. 13-19. Due to symmetric fibre orientations of the composite, the

horizontal and vertical displacements distributions are same for top and bottom plies. As expected, the displacement in the thickness direction, the top and bottom plies have deformation in the opposite direction. The transverse displacement of the middle ply is observed as zero. It can be inferred from Fig. 17 and 19 that a delamination tendency exists on the right side due to higher temperatures. Good agreements are also obtained with ANSYS solutions.

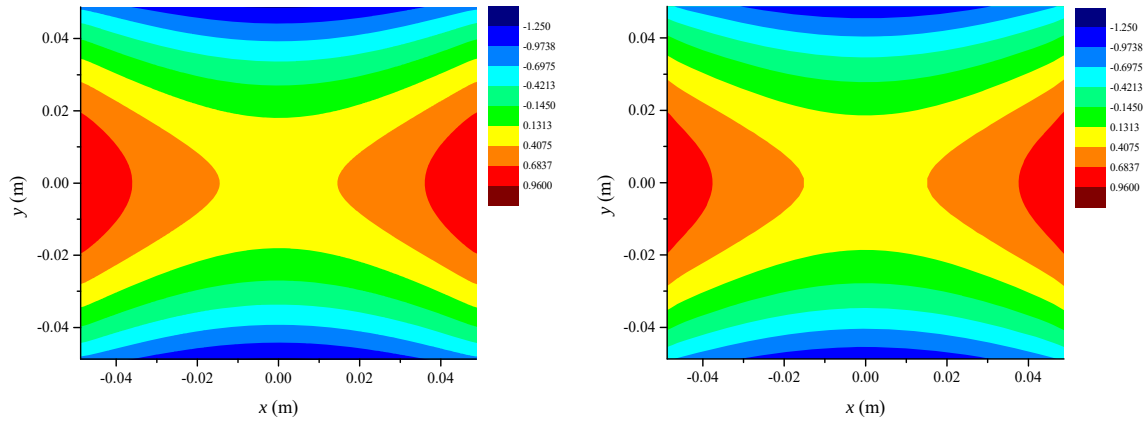

(a) (b)

Fig. 13. Horizontal displacements, $u_x\ (\mu m)$ (a) PD (b) ANSYS results for bottom ply.

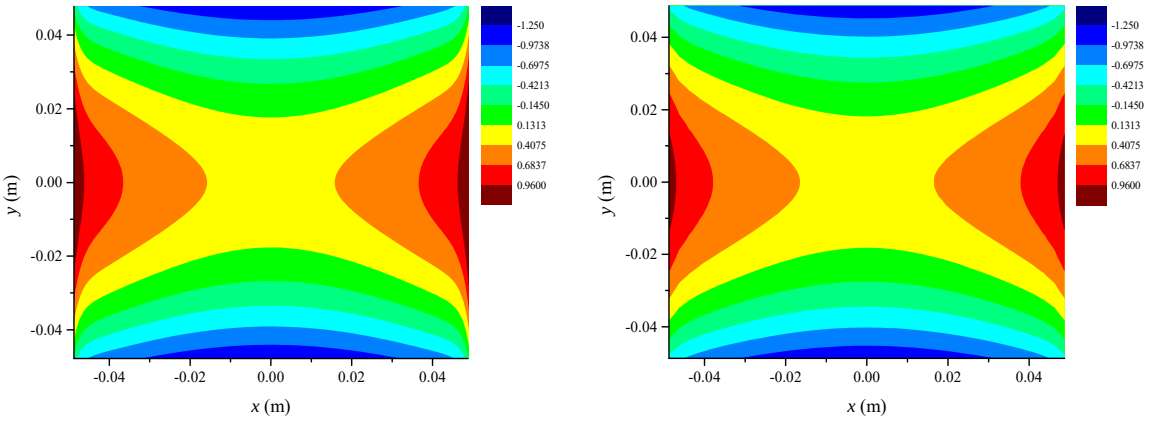

(a) (b)

Fig. 14. Horizontal displacements, $u_x\ (\mu m)$ (a) PD (b) ANSYS results for middle ply

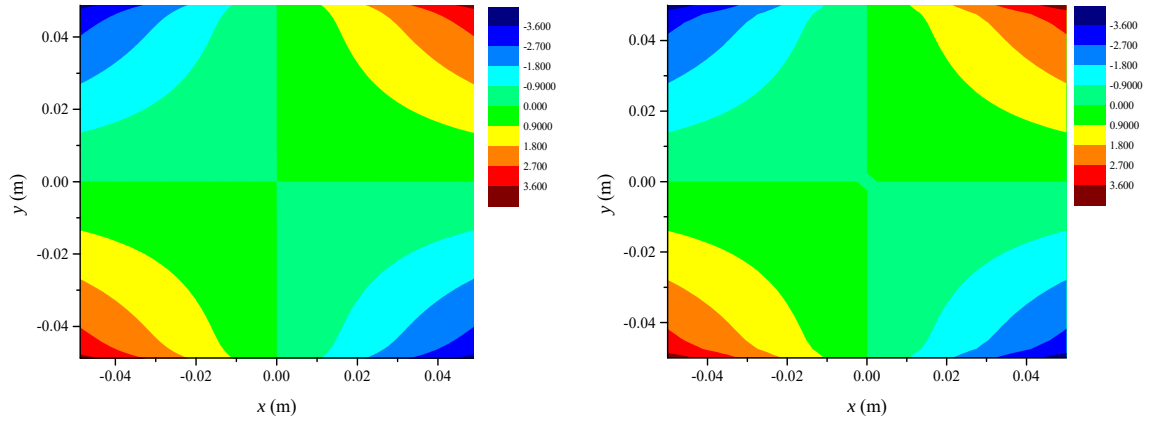

(a) (b)

Fig. 15. Vertical displacements, u_y (μm) (a) PD (b) ANSYS results for bottom ply.

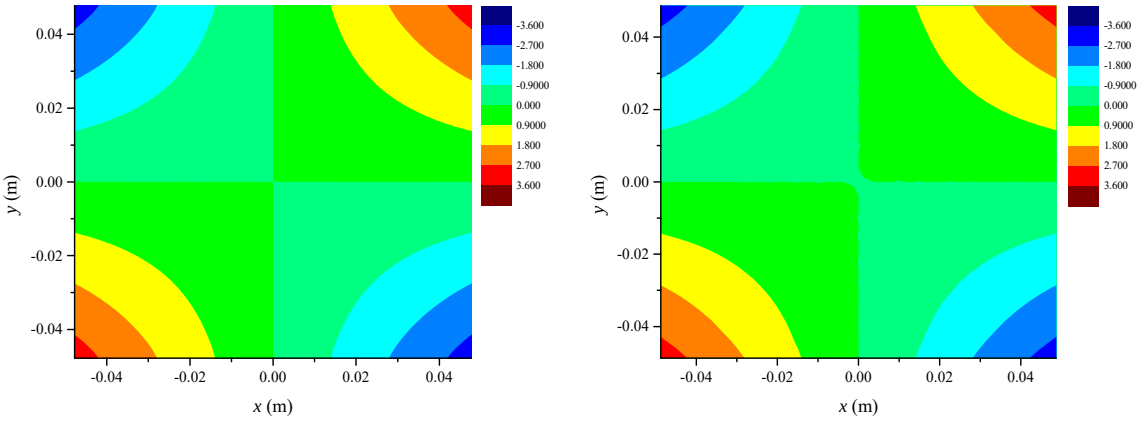

(a) (b)

Fig. 16. Vertical displacements, u_y (μm) (a) PD (b) ANSYS for middle ply.

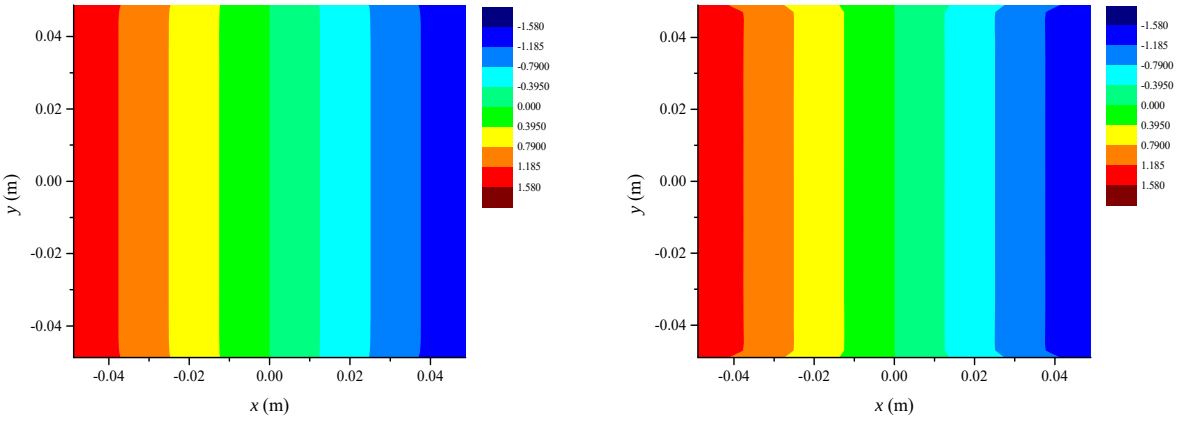

(a) (b)

Fig. 17. Transverse displacement, u_z (μm) (a) PD (b) ANSYS for bottom ply.

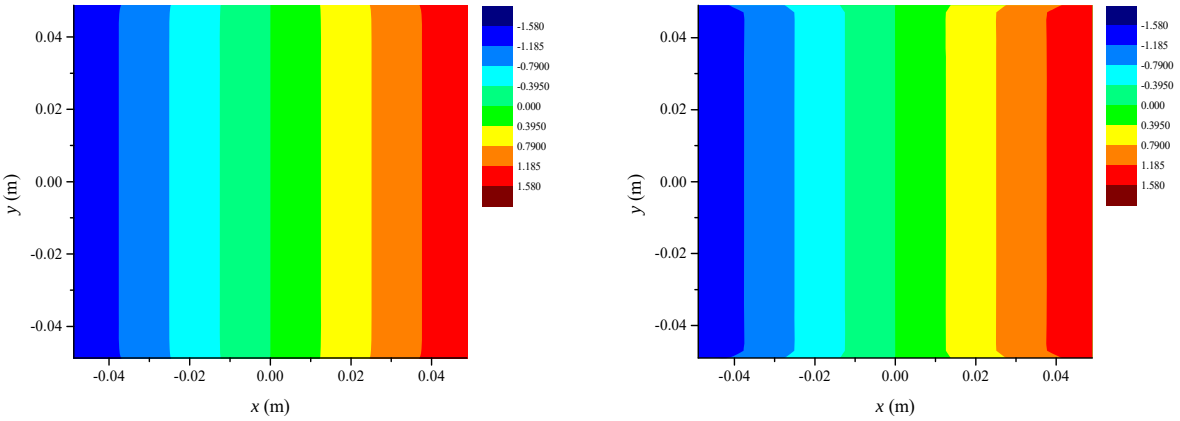

(a) (b)

Fig. 18. Transverse displacement, $u_z\ (\mu\text{m})$ (a) PD (b) ANSYS for top ply.

4.2 Heat transfer in composites

In this section, pure heat transfer analyses in single and multi-layer composite model are tested in order to validate the proposed multi-layer PD thermal model.

4.2.1 Composite subject to heat flux on top ply

Constant heat flux of $5000\ \text{W/m}^2$ is applied on the top ply of the multi-layer model. The composite model is initially at reference temperature, Θ_0. The total simulation time is $t = 50\ \text{s}$ and the time step size in PD solution is defined as $\text{d}t = 0.01\ \text{s}$. On the other hand, the element type SOLID278 is utilized in the transient thermal ANSYS analysis. A grid 60×60 in the x-y plane with three elements in the z direction is chosen in the ANSYS model. In addition, the time step size used in ANSYS model is $2.5\ \text{s}$. The temperature change distribution predictions during the simulation process are compared with those

from ANSYS simulation, as shown in Fig. 19-22. The remarkable match indicates the successful application of the PD interlayer heat flow formulation.

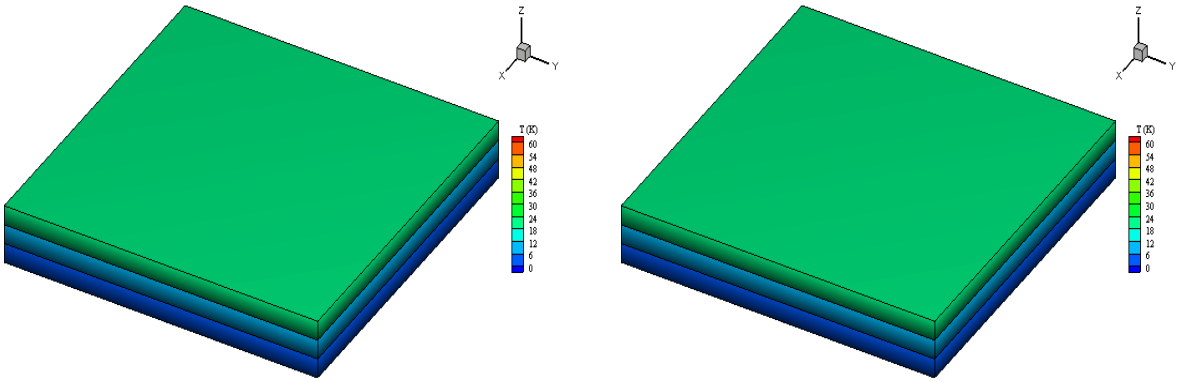

(a) (b)

Fig. 19. Temperature change distributions at $t = 10$ s (a) PD (b) ANSYS results

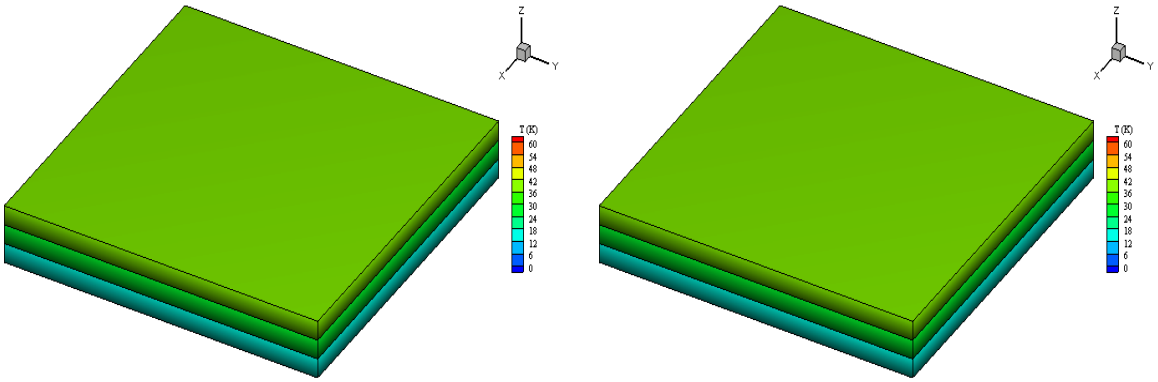

(a) (b)

Fig. 20. Temperature change distributions at $t = 30$ s (a) PD (b) ANSYS results

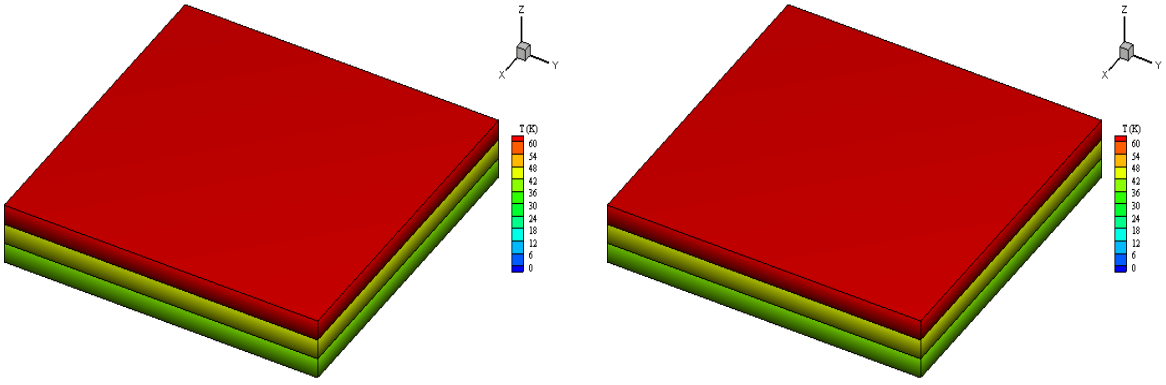

(a) (b)

Fig. 21. Temperature change distributions at $t = 50$ s (a) PD (b) ANSYS results

4.2.2 Composite subject to temperature boundary condition

In order to verify the PD heat conduction model for in-plane and transverse directions, a temperature boundary condition $\Delta T = \left(y + 100z\right)t\,\left(\mathrm{K}\right)$ is applied at $x = -L/2$, where x, y and z represent the coordinate components and t is the simulation time. The composite model is initially at reference temperature, Θ_0. The total simulation time is $300\ \mathrm{s}$ and the time step size in PD solution is $\mathrm{d}t = 0.01\ \mathrm{s}$. The SOLID278 element type is chosen for the ANSYS model with time step size $10\ \mathrm{s}$. The ANSYS model is constructed with 40 elements in x and y directions and 3 elements in z direction. The PD results of temperature distributions are compared with the ANSYS solutions, as shown in Fig. 22-25. Good agreement is achieved, thus the PD thermal model of the laminate is validated.

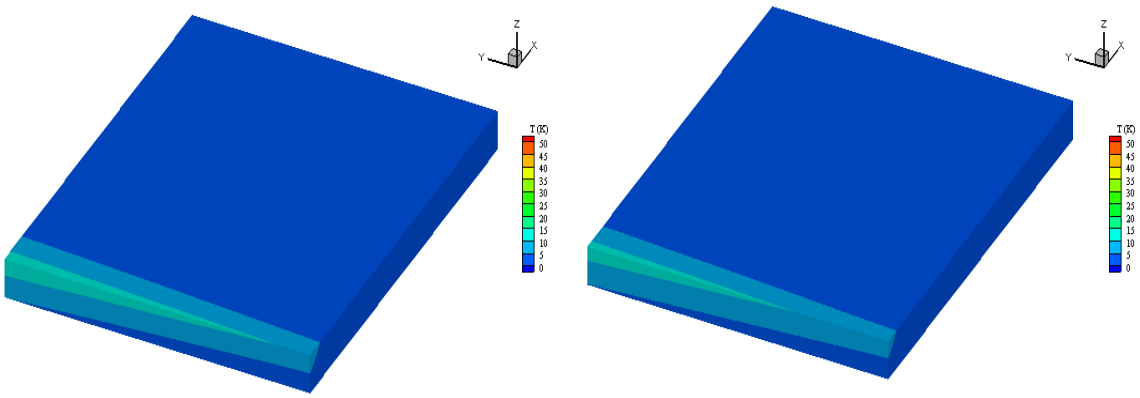

(a) (b)

Fig. 22. Temperature change distributions at $t = 50$ s (a) PD (b)ANSYS results

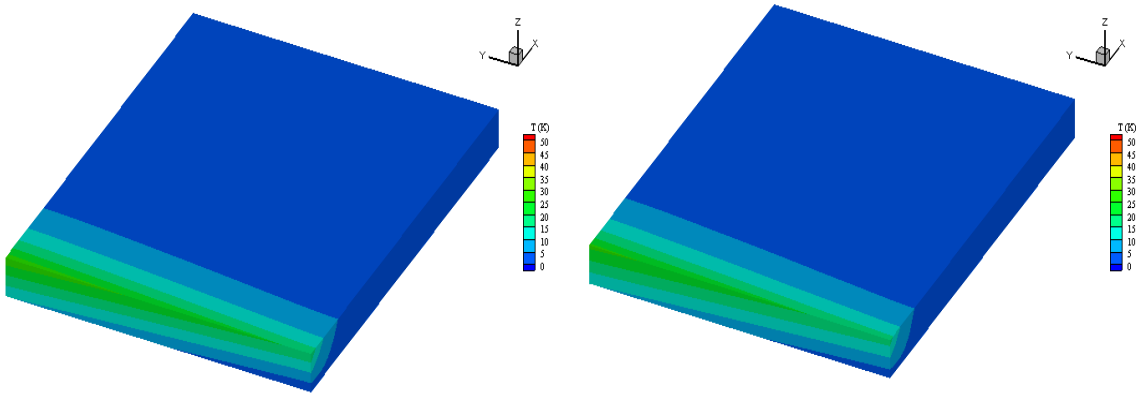

(a) (b)

Fig. 23. Temperature change distributions at $t = 100$ s (a) PD (b) ANSYS results

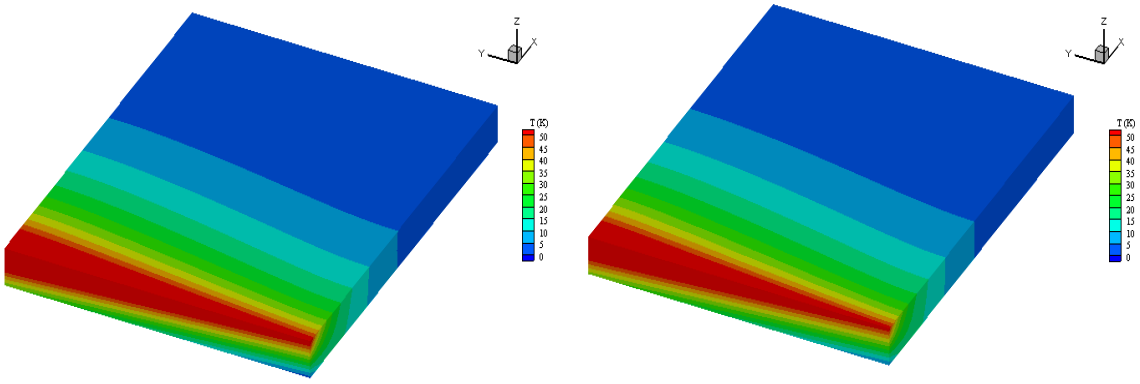

(a) (b)

Fig. 24. Temperature change distributions at $t = 300$ s (a) PD (b) ANSYS results.

4.3 Composites subject to pressure shock

In order to validate the fully coupled thermomechanical PD formulations, the deformation and thermal responses of single layer and multi-layer composite models under pressure shock loads are

investigated. As illustrated in Fig. 25, the plate is fixed on the right edge and it is subjected to pressure loading on the left edge. The plate is insulated at the top, bottom and right edges.

The initial conditions are:

$$u_x\left(x,y,z,t=0\right)=u_y\left(x,y,z,t=0\right)=u_z\left(x,y,z,t=0\right)=0 \tag{32a}$$

$$T\left(x,y,z,t=0\right)=0 \tag{32b}$$

The boundary conditions are:

$$u_x\left(x=L/2,\,y,\,z,\,t\right)=u_y\left(x=L/2,\,y,\,z,\,t\right)=u_z\left(x=L/2,\,y,\,z,\,t\right)=0 \tag{33a}$$

$$\sigma_{xx}\left(x,\,y=\pm W/2,\,z,\,t\right)=\sigma_{yy}\left(x,\,y=\pm W/2,\,z,\,t\right)=\sigma_{zz}\left(x,\,y=\pm W/2,\,z,\,t\right)=0 \tag{33b}$$

$$\sigma_{xx}\left(x=-L/2,y,t\right)=P\left(t\right) \tag{33c}$$

$$T_{,x}\left(x=\pm L/2,\,y=\pm W/2,\,z,\,t\right)=0 \tag{33d}$$

$$T_{,y}\left(x=\pm L/2,\,y=\pm W/2,\,z,\,t\right)=0 \tag{33e}$$

$$T_{,z}\left(x=\pm L/2,\,y=\pm W/2,\,z,\,t\right)=0 \tag{33f}$$

where u_z represents the displacement in z direction.

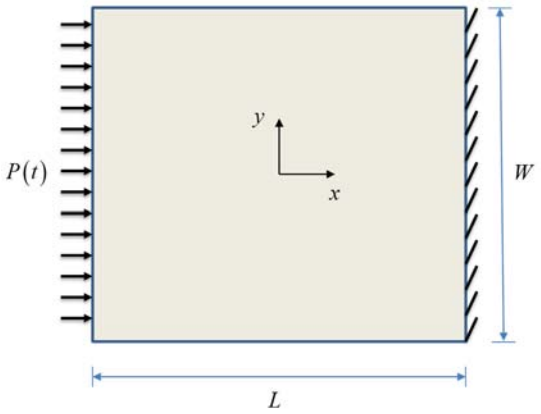

Fig. 25. The top view of composite models under a pressure shock.

4.3.1 Single layer composite subject to pressure shock

Pressure shock loading is applied to the single layer composite model for 2 different cases.

Case 1:

$$P\left(t\right)=10^{10}\sin\left(\pi t\times10^{6}\right)\text{ Pa; for fibre angle }\Phi=0^{o} \tag{34a}$$

Case 2:

$$P\left(t\right)=-10^{14}t\text{ Pa; for fibre angle }\Phi=90^{o} \tag{34b}$$

The induced temperature changes and horizontal displacements along the central line of the ply are predicted with the newly developed fully coupled thermomechanical model. The results are compared with ANSYS solutions by using directly coupled method [44]. The directly coupled element

PLANE223 is utilized in the transient thermomechanical analysis. The mesh size is 2×10^{-4} m and the time step size is 8×10^{-8} s in ANSYS solution.

Fig. 26 and Fig. 27 provide the temperature change distributions and horizontal displacements for 2 different cases. In case 1, a compressive wave is generated. As the wave moves to the right, temperature rise is observed where there is local compression, on the other hand temperature drop is observed where there is local tension. On the other hand, in case 2 temperature drop is observed due to applied tension loading. The observed temperatures coincide with the theory and experimental results [45]. As seen from Fig. 26-28, the induced temperature changes and horizontal displacements match very well with ANSYS solutions.

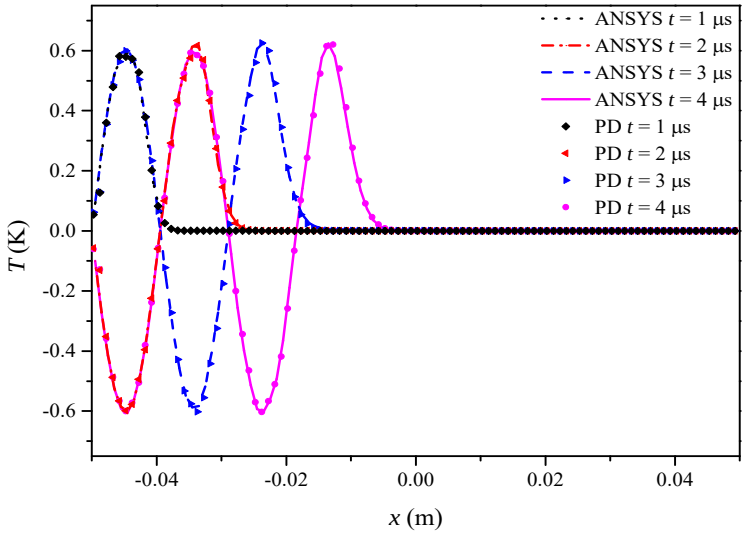

(a)

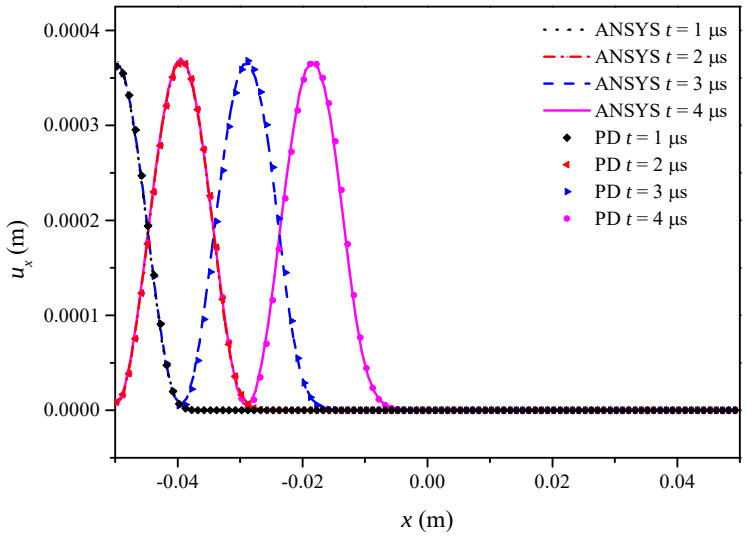

(b)

Fig. 26. (a) Temperature change distributions (b) horizontal displacements at $y = 0$ for case 1

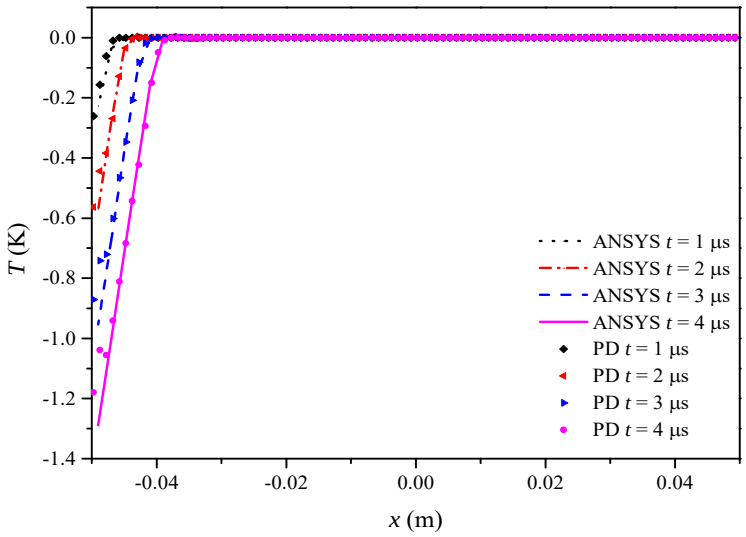

(a)

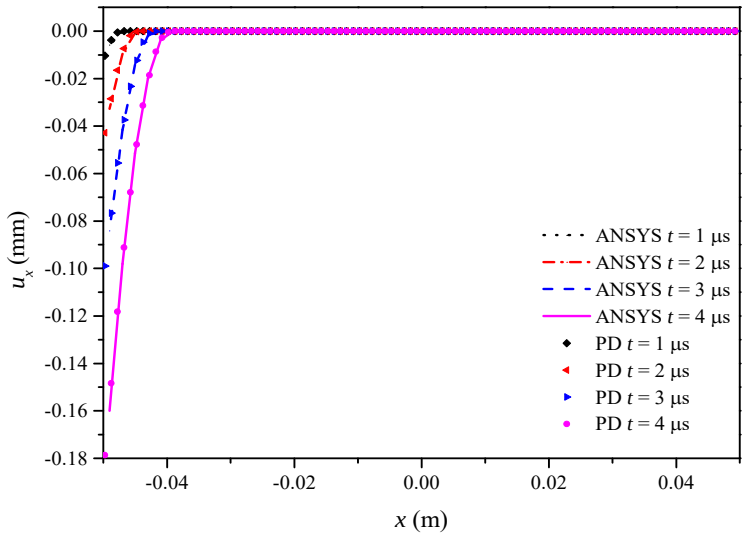

(b)

Fig. 27. (a) Temperature change distributions (b) horizontal displacements at $y = 0$ for case 2

4.3.2 Multi-layer composite subject to pressure shock

In order to validate the proposed PD fully coupled thermomechanical model for multi-layer composites, a pressure shock loading is applied on the multi-layer model as:

$$P(t) = -10^{16} t \text{ Pa} \tag{35a}$$

The induced temperature changes and displacements along the central lines of all three plies are predicted with the proposed PD model. Furthermore, the results are compared ANSYS solutions by using coupled element type SOLID226. The mesh size and time step remain same with the ones from the multi-layer composite as in section 4.1.1.

Fig. 28 and Fig. 29 are the horizontal displacements and temperature change distributions of each ply, respectively. Due to the symmetry stacking sequence and loading condition, the top ply and bottom behave similarly. As it can be seen in Fig. 28, the displacements of the middle ply is slightly larger than

the bottom ply due to fibre orientation since the fibres in the middle ply are perpendicular to the loading direction, on the other hand the fibres in the top and bottom plies are in the loading direction. Similarly, in terms of the temperature field, temperature changes of the middle ply are also much larger than the bottom ply as seen in Fig. 29. As the time progresses, sudden temperature variations are observed near the boundary. Although there are little discrepancies between the PD and ANSYS results in the later stage especially in the middle ply, such variations are also captured in PD results.

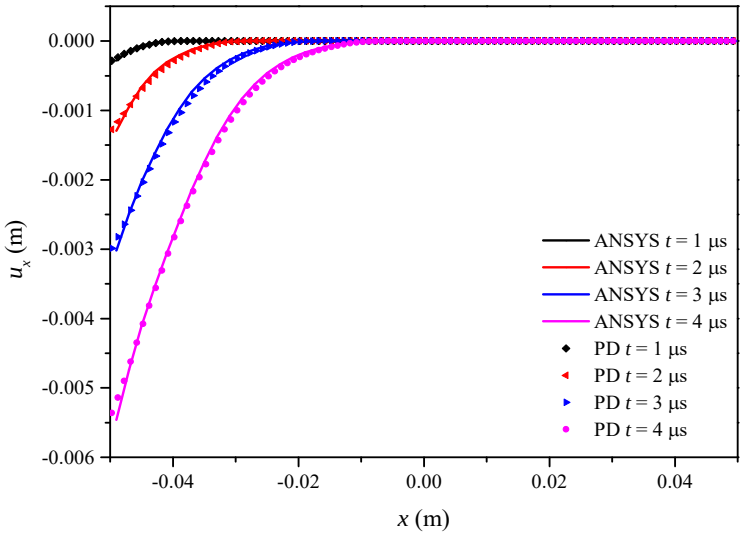

(a)

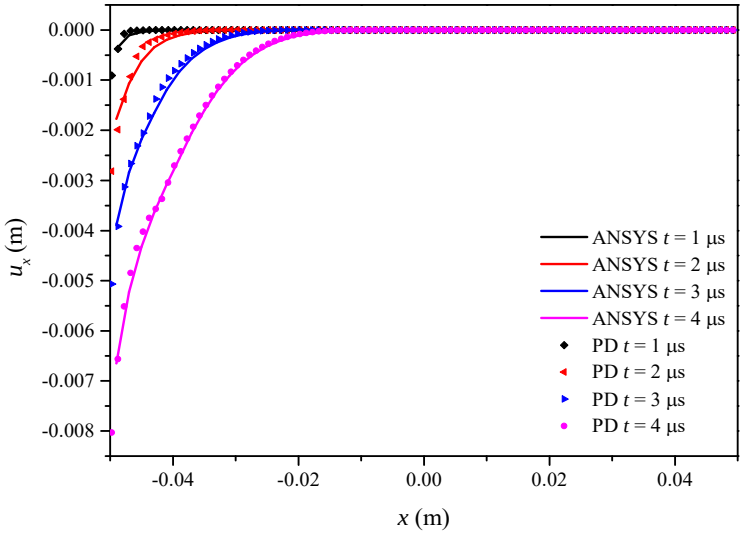

(b)

Fig. 28. Horizontal displacements at $y = 0$ (a) bottom ply (b) middle ply

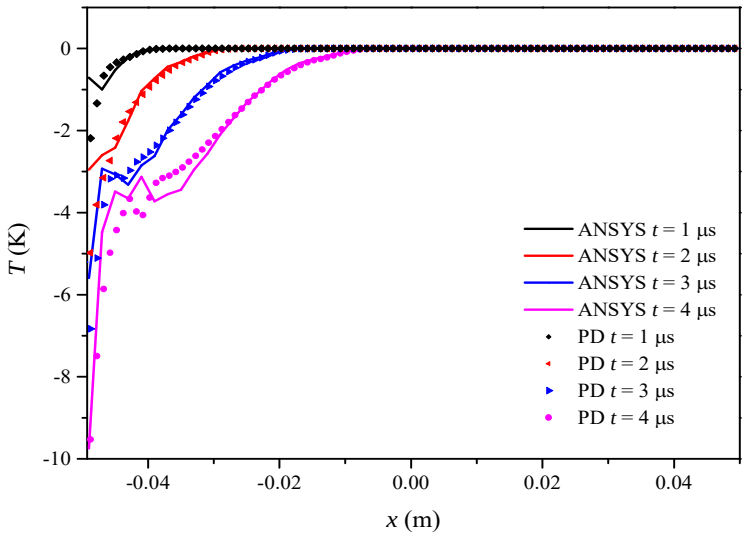

(a)

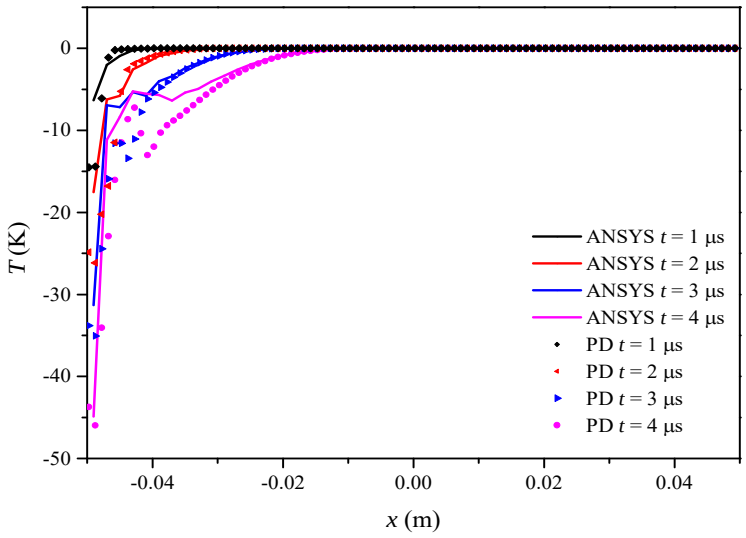

(b)

Fig. 29. Temperature change distributions at $y = 0$ (a) bottom ply (b) middle ply

4.4 Crack propagation predictions of composites

After verifying the developed PD themomechanical formulations for both single and multi-layer composites, in this section, damage patterns and corresponding temperature change distributions for single layer and multi-layer composite model at different integration times are presented with pre-existing crack size of $2a = 2.0\,\text{cm}$ as seen in Fig. 30. The initial and boundary conditions are identical to those from section 4.3. PD discretization is achieved with a uniform grid of 300×300. The critical stretch values are calculated as $s_m = 0.0177$ and $s_{in} = 0.03734$ with $G_{IC} = 2.37 \times 10^{-3}$ MPa/m [15]. The critical stretch value of fibre bond is assumed to be twice the matrix bond, i.e $s_f = 0.0354$. The

critical stretch value of interlayer shear bonds is calculated as $\phi_c = 0.1043$ with $G_{IIC} = 7.11\times10^{-3}$ MPa/m [37]. The simulation time is chosen as $14\ \mu s$ with time step size 10^{-9} s.

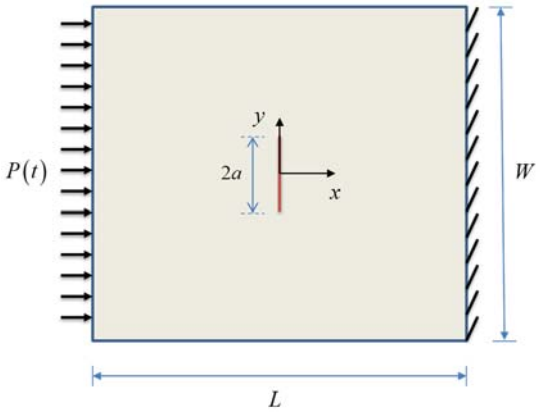

Fig. 30. Top view of a composite model with a central crack under a tension pressure shock.

4.4.1 Single layer composite with a central crack

Pressure shock loading is applied to the single layer composite with a crack for 2 different cases.

Case 1:

$$P(t) = -3\times10^{14}\left(tH(t_0 - t) + t_0 H(t - t_0)\right) \text{ Pa; for fibre direction } \Phi=0^{o} \quad (36a)$$

Case 2:

$$P(t) = -5\times10^{12}\left(tH(t_0 - t) + t_0 H(t - t_0)\right) \text{ Pa; for fibre direction } \Phi=90^{o} \quad (36b)$$

where $t_0 = 4.0\ \mu s$.

The damage plots and temperature change distributions at different time steps are provided in Fig. 31-34 for case 1. As shown in Fig. 31(a), the crack begins to propagate at $t = 8\ \mu s$. Coinciding with the predictions in previous solutions [18, 19], the crack grows along the fibre direction which is perpendicular to the pre-existing crack direction. From this figure, it can also be noticed that the cracks on either side of the pre-existing crack tips grow equally. It indicates the fibre/matrix debonding [46] failure mode, which arises from in-plane shear stress in the matrix. A similar failure pattern is observed in the experiments conducted by Bogert et al.[47]. As presented in Fig. 33(b), temperature increases near the crack, which agrees with the conclusion in [48]. There is a temperature drop due to local tension near the crack tip. On the other hand, there is a temperature rise along the crack surfaces due to local compression. The temperature change distribution has a similar pattern as the crack growth.

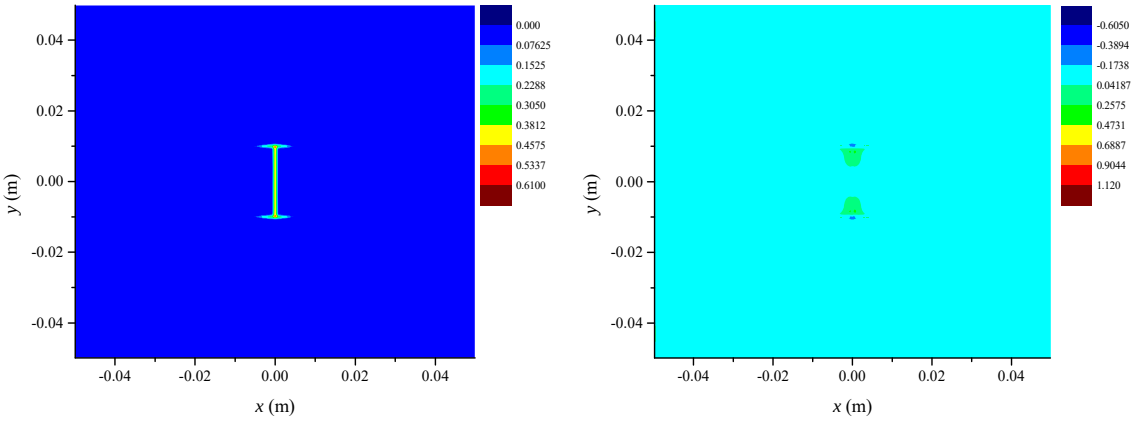

(a) (b)

Fig. 31. (a) Matrix damage plot (b) Temperature change distributions (K) for case 1 at $t = 8\,\mu\mathrm{s}$.

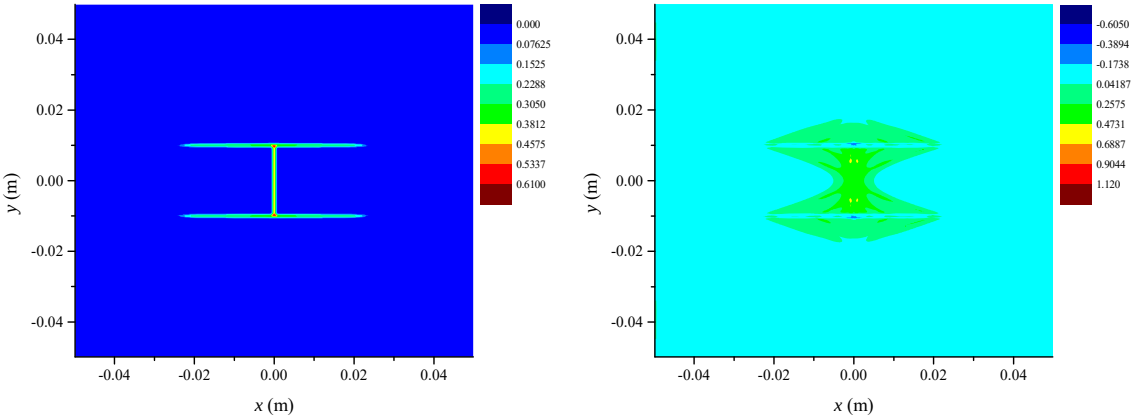

(a) (b)

Fig. 32. (a) Matrix damage plot (b) Temperature change distributions (K) for case 1 at $t = 11\,\mu\mathrm{s}$.

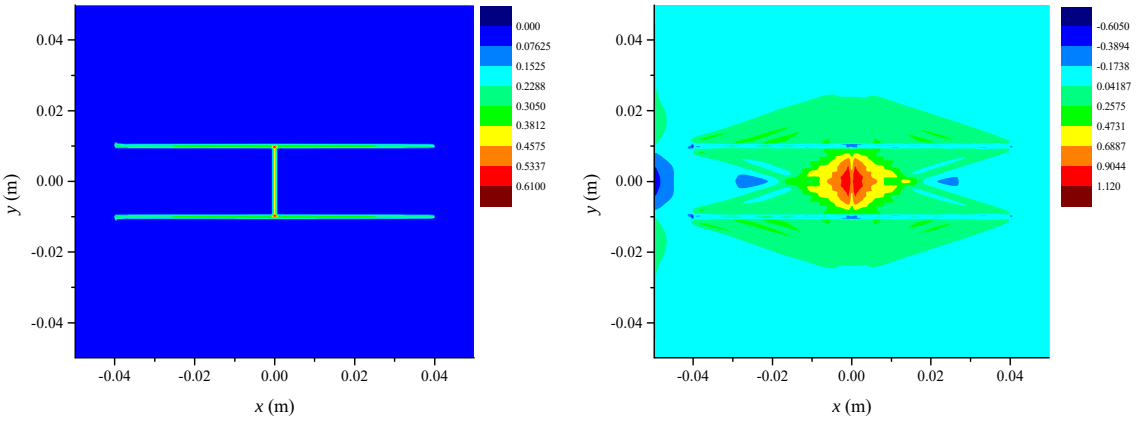

(a) (b)

Fig. 33. (a) Matrix damage plot (b) Temperature change distributions (K) for case 1 at $t = 14\,\mu\mathrm{s}$.

The crack growth and temperature change predictions at different time steps are provided in Fig. 34-37 for case 2. Similar to case 1, the crack propagates along the fibre direction, indicating the fibre/matrix debonding. Only the splitting failure mode is observed in the PD prediction, which is consistent with

the experimental observations from [49, 50]. The temperature drops at crack tips are observed in Fig. 34-37.

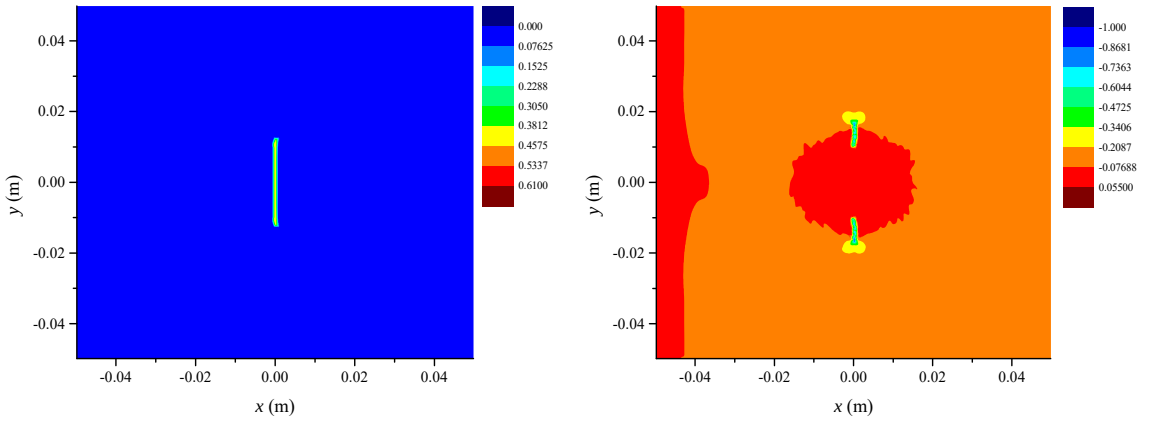

(a) (b)

Fig. 34. (a) Matrix damage plot (b) Temperature change distributions (K) for case 2 at $t = 7.5\mu\mathrm{s}$

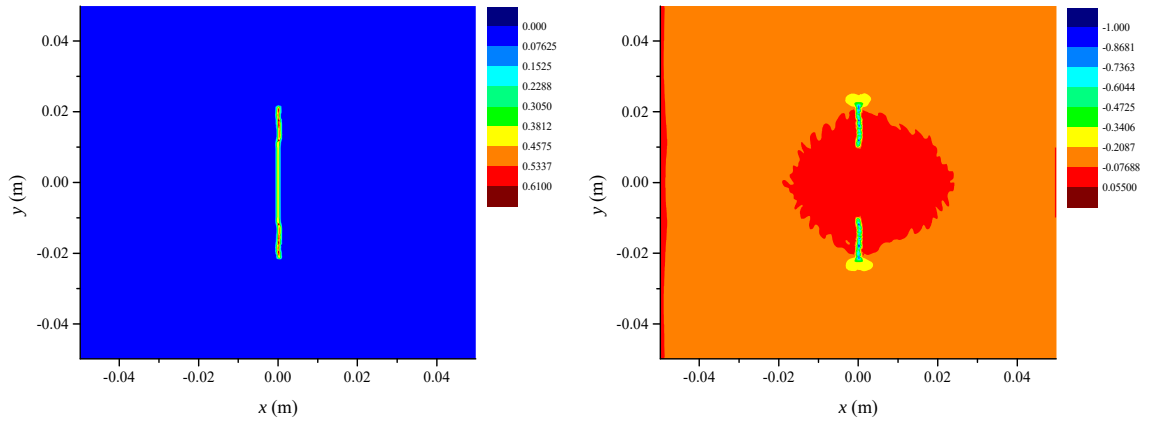

(a) (b)

Fig. 35. (a) Matrix damage plot (b) Temperature change distributions (K) for case 2 at $t = 8\mu\mathrm{s}$.

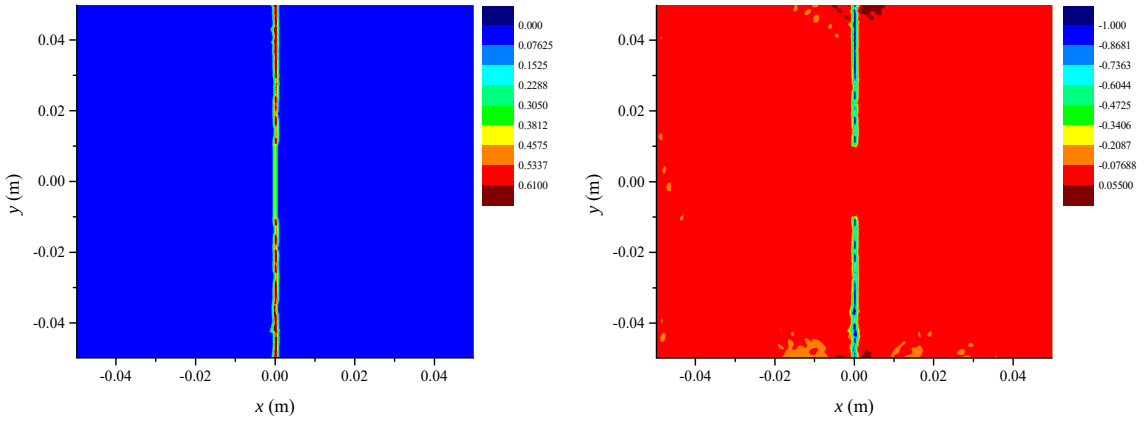

(a) (b)

Fig. 36. (a) Matrix damage plot (b) Temperature change distributions $\left(\mathrm{K}\right)$ for case 2 at $t = 10.5\,\mu\mathrm{s}$.

4.4.2 Multi-layer composite with a central crack

In this section, the crack propagation in multi-layer composite is investigated. The load that is applied to investigate the damage pattern is given as;

$$P\left(t\right) = -3\times10^{14}\left(tH\left(t_0 - t\right) + t_0 H\left(t - t_0\right)\right)\ \mathrm{Pa} \tag{37}$$

with $t_0 = 4\,\mu\mathrm{s}$.

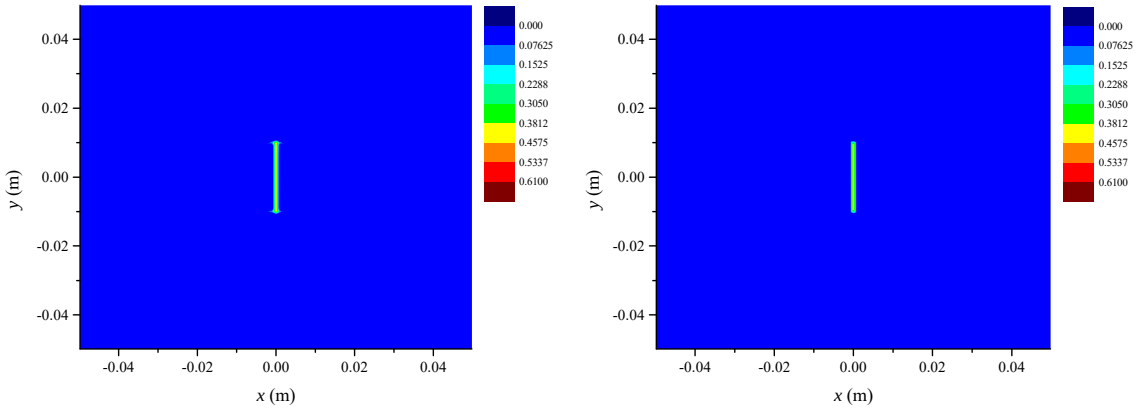

(a) (b)

Fig. 37. Matrix damage plot of (a) bottom ply and (b) middle ply at $t = 8\,\mu\mathrm{s}$.

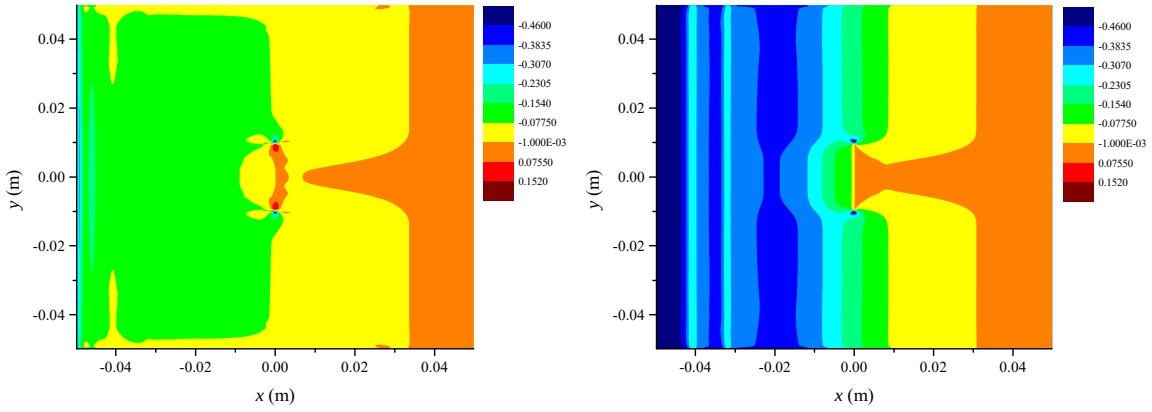

(a) (b)

Fig. 38. Temperature change distributions (K) for (a) bottom ply and (b) middle ply at $t = 8\,\mu\mathrm{s}$.

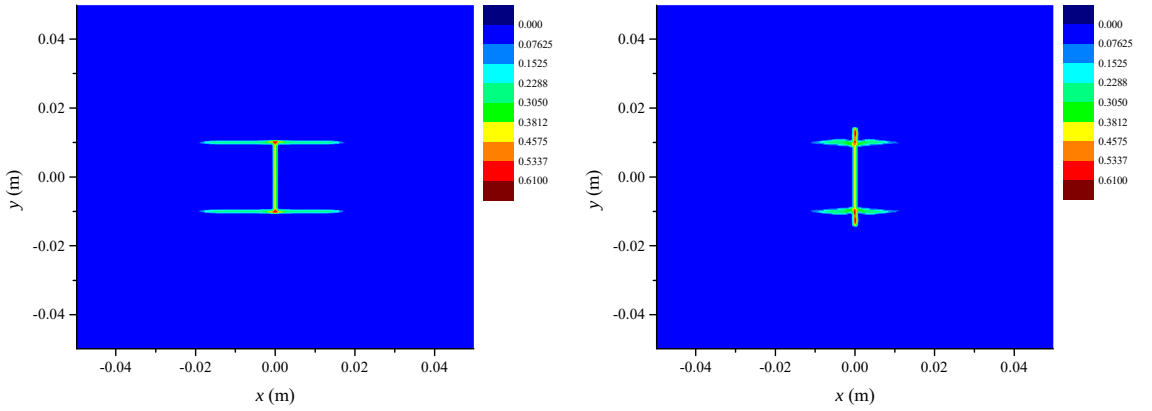

(a) (b)

Fig. 39. Matrix damage plot of (a) bottom ply and (b) middle ply at $t = 11\,\mu\mathrm{s}$.

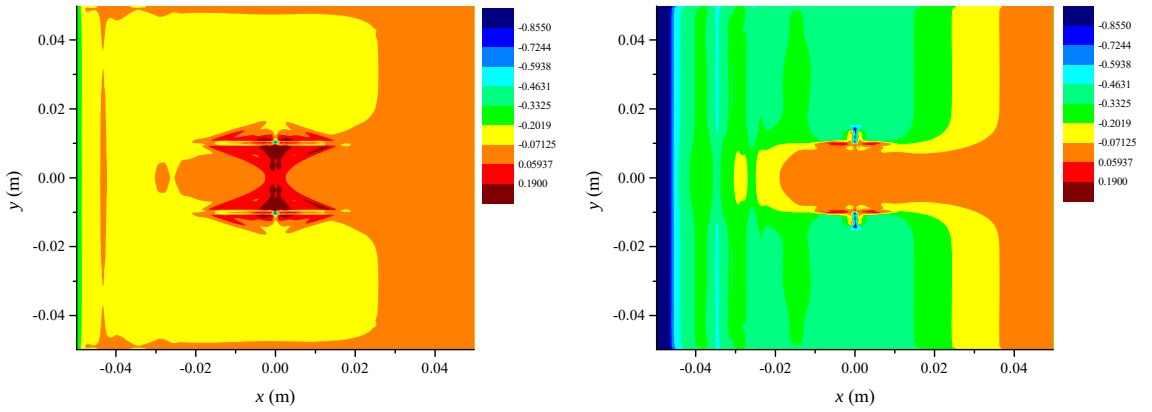

(a) (b)

Fig. 40. Temperature change distributions (K) for (a) bottom ply and (b) middle ply at $t = 11\,\mu\mathrm{s}$.

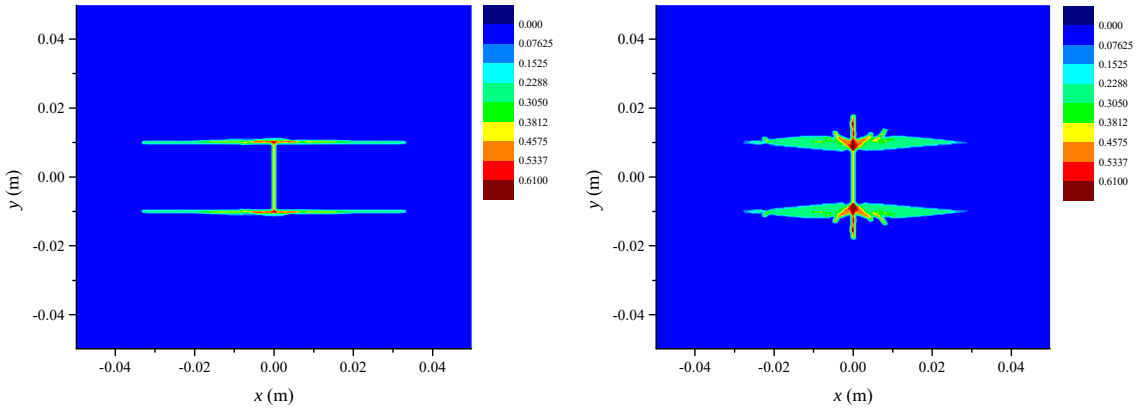

(a) (b)

Fig. 41. Matrix damage plot of (a) bottom ply and (b) middle ply at $t = 14\,\mu s$.

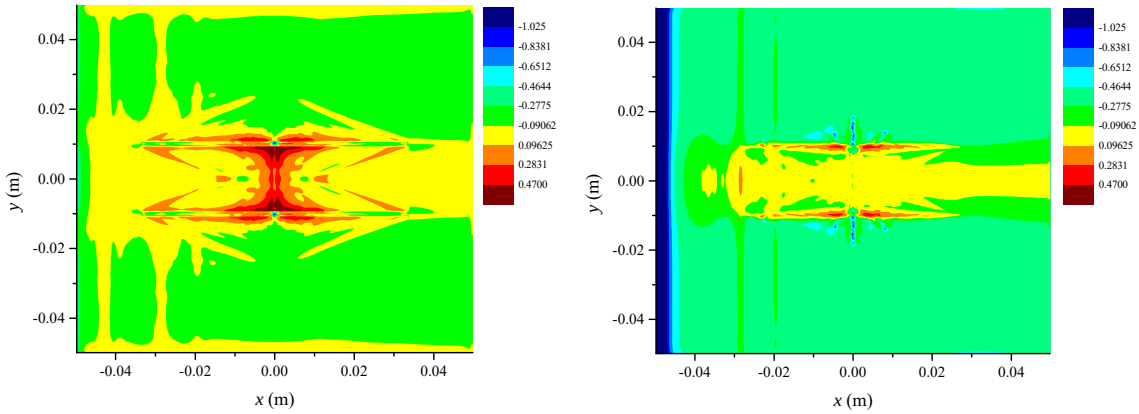

(a) (b)

Fig. 42. Temperature change distributions (K) for (a) bottom ply and (b) middle ply at $t = 14\,\mu s$.

The damage plots for in-plane matrix bonds and their corresponding temperature change distributions at different time steps are presented in Fig. 37-43. For the laminate, an "H" type splitting failure mode is observed for all plies, which agrees with the findings in [15] and the experimental results in [51]. It is observed that the matrix breakage in top or bottom ply shown in Fig. 41 (a) is similar to damage pattern obtained for a single layer composite model with $\Phi = 0^{\circ}$ fibre direction as shown in Fig. 33 (a). However, as shown in Fig. 41 (b), the middle ply apparently has a bigger damage zone than the other two plies, which is consistent with the conclusions in [52]. This is due to alignment of the fibres. Since the fibres are not aligned with the loading direction in the middle ply, the extent of damage is bigger than other two layers. This is also indicating the different damage levels in multi-layer composites. Furthermore, the crack grows both in the fibre direction and in the transverse direction in the middle ply, presenting a different crack growth path compared with the predictions from the analysis of single layer composite model with fibre direction $\Phi = 90^{\circ}$ as shown in Fig. 36 (a). As a result, a complex damage mode is presented in the middle ply [46]. The interaction between the plies is taken into account

through interlayer bonds. It is also observed that the crack pattern has an influence on the induced temperature distribution.

5 Conclusion

In this paper, a fully coupled thermomechanical model formulated by ordinary state based peridynamic theory is proposed both for single layer and multi-layer composites. Subsequently, numerical simulations of some benchmark problems are conducted for the validation of the developed model. The temperature and deformation fields are investigated by considering the coupling effects in both fields. Consequently, the present model is validated by comparing peridynamic simulations with ANSYS results. Finally, failure analyses are conducted with pre-existing cracks on single layer and multi-layer models. The progressive crack propagations and temperature distribution evolutions are discussed. The following conclusions can be drawn:

1. The present model in the framework of ordinary state based peridynamic theory is capable of predicting the deformation of multi-layer composites under thermal loads.
2. The developed PD thermal model can be applied in heat conduction simulations for multi-layer composites.
3. The proposed fully coupled ordinary state based thermomechanical model can be applied to predict the crack propagation for composites. The induced temperature distribution evolution can also be predicted.

Acknowledgements

The authors gratefully acknowledge financial support from China Scholarship Council (CSC No. 201506230126) and University of Strathclyde.

Appendix A

PD thermal micro conductivities for composites

The heat conduction equation for a single layer composite provided by Oterkus and Madenci [21] is modified for multi-layer composites as

$$\begin{aligned}\rho c_v \dot{T}_k^n = &\sum_{j=1}^{N_{ply}}\left[\left(\mu_f\kappa_f+\kappa_m\right)\frac{\Theta\left(\mathbf{x}_j^n,t\right)-\Theta\left(\mathbf{x}_k^n,t\right)}{\left|\mathbf{x}_j^n-\mathbf{x}_k^n\right|}\right]V_j^n \\ &+\sum_{m=n+1,n-1}\sum_{j=1}^{N_{inter}}\left[\kappa_{inter}\frac{\Theta\left(\mathbf{x}_j^m,t\right)-\Theta\left(\mathbf{x}_k^n,t\right)}{\left|\mathbf{x}_j^m-\mathbf{x}_k^n\right|}\right]V_j^m+\rho q_b\left(\mathbf{x}_k^n,t\right)\end{aligned} \tag{A.1}$$

The first term on the right side of Eq. (A.1) represents the in-plane heat conduction in a lamina [21] and the second term represents the heat conduction between the neighbouring layers.

The PD thermal micro conductivities can be determined by applying simple loading conditions and by comparing thermal potentials with classical formulations [23, 28]. The thermal micro conductivities for a lamina provided by Oterkus and Madenci [21] are given in Eq. (12). Similarly, the thermal micro conductivity through the thickness direction can be calculated by applying simple loading condition as

$$\Theta\left(x,y,z\right)=z \tag{A.2}$$

The thermal potential in classical formulation can be calculated under the given loading condition as [23, 28, 30]

$$Z_C=\frac{1}{2}k_m\left(\frac{\partial\Theta}{\partial z}\right)^2=\frac{1}{2}k_m \tag{A.3}$$

where k_m is the thermal conductivity in the thickness direction. In a resin-rich laminate, the material property in the thickness direction can be assumed to be same with the matrix material property.

The corresponding PD thermal micropotential developed by the central point $\mathbf{x}$ and its family member $\mathbf{x}'$ can be evaluated as [23]

$$z_{PD}=\kappa_{inter}\frac{\left[\Theta-\Theta'\right]^2}{2\left|\mathbf{x}-\mathbf{x}'\right|} \tag{A.4}$$

The PD thermal potential is the summation of all microthermal potential with the point, calculated as

$$Z_{PD}=\frac{1}{2}\int_H\kappa_{inter}\frac{\left[\Theta-\Theta'\right]^2}{2\left|\mathbf{x}-\mathbf{x}'\right|}\mathrm{d}V' \tag{A.5}$$

where κ_{inter} is the PD thermal bond constant in the thickness direction. The integration domain, H, for the interlayer thermal bonds between n^{th} ply and m^{th} ply is a circle disk with thickness being equal to h. For the given loading condition, the temperature difference becomes

$$\Theta'-\Theta=h \tag{A.6}$$

Therefore, Eq.(A.5) can be evaluated as

$$Z_{PD} = 2\left(\frac{1}{2}\int_0^{2\pi}\int_0^{\delta}\kappa_{inter}\frac{h^2}{2\sqrt{|\xi'|^2+h^2}}h|\xi'|d|\xi'|d\varphi\right) = \pi\kappa_{inter}h^3\left(\tilde{\delta}-h\right) \tag{A.7}$$

where ξ' represents the projection of the relative position ξ on the layer in which **x** is located, i.e. $|\xi| = \sqrt{|\xi'|+h^2}$. By equating the thermal potential from both from the classical theory Eq.(A.3) and peridynamic theory Eq.(A.7), the peridynamic bond constant for interlayer interactions can be found as

$$\kappa_{inter} = \frac{k_m}{2\pi h^3\left(\tilde{\delta}-h\right)} \tag{A.8}$$

where $\tilde{\delta}$ is the horizon for interlayer shear bonds with $\tilde{\delta} = \sqrt{\delta^2+h^2}$ (see Fig. 6(b)).

Appendix B

PD thermal modulus for composites

B.1 Free Energy density

The free energy density in classical continuum mechanics for small deformation can be represented by summation of internal energy density or strain energy and dissipated energy density into heat [53] as

$$\Psi_{CCM} = W^M_{CCM} - W^T_{CCM} \tag{B.1a}$$

with

$$W^M_{CCM} = \frac{1}{2}\{\sigma\}\{\varepsilon\} \tag{B.1b}$$

$$W^T_{CCM} = \left[\{\beta_{cl}\}\{\varepsilon\}T + \frac{c_v}{2\Theta_0}T^2\right] \tag{B.1c}$$

where $\{\beta_{cl}\}$ is the thermal modulus vector in classical continuum mechanics, $\{\sigma\}$ is the stress tensor, $\{\varepsilon\}$ is the strain vector and Ψ_{CCM} is the free energy density. Similarly, the PD free energy density can be written [24] as

$$\Psi_{PD} = W^M_{PD} - W^T_{PD} \tag{B.2a}$$

where

$$W^M_{PD} = \frac{1}{2}\underline{\mathbf{U}}\bullet\mathbb{K}\bullet\underline{\mathbf{U}} \tag{B.2b}$$

$$W_{PD}^{T}=\left[\underline{\mathbf{B}}\bullet\underline{\mathbf{U}}T+\frac{c_v}{2\Theta_0}T^2\right] \tag{B.2c}$$

where $\underline{\mathbf{B}}$ is the thermal modulus and $\underline{\mathbf{U}}$ is the displacement in PD theory. Also, $\mathbb{K}$ is the modulus state [54]. Eq. (B.1c) and (B.2c) include the coupling term between mechanical and thermal field.

PD mechanical model is developed by equating the strain energy densities from both theories as [19, 30, 55, 56]

$$W_{CCM}^{M}=W_{PD}^{M} \tag{B.3}$$

Similarly, PD thermal modulus can be found by equating the free energy densities i.e. $\Psi_{CCM}=\Psi_{PD}$, which results in

$$W_{CCM}^{T}=W_{PD}^{T} \tag{B.4}$$

B.2 PD thermal modulus expression for single layer/ lamina model

The peridynamic representation of thermal modulus is determined by applying 2 simple loading conditions as:

Loading 1:

$$\varepsilon_{11}=\zeta,\ \varepsilon_{22}=\gamma_{12}=0 \tag{B.5a}$$

Loading 2:

$$\varepsilon_{22}=\zeta,\ \varepsilon_{11}=\gamma_{12}=0 \tag{B.5b}$$

According to CCM:

In classical continuum mechanics, with respect to the material coordinate system, the thermal modulus for a lamina is defined as

$$\{\beta_{cl}\}=[Q]\{\alpha\} \tag{B.6}$$

where $[Q]$ is the reduced stiffness matrix given as provided in Eq. (11a). The thermal expansion coefficient vector, $\{\alpha\}$, is defined as

$$\{\alpha\}=\begin{Bmatrix}\alpha_1\\ \alpha_2\\ 0\end{Bmatrix} \tag{B.7}$$

Under the given two loading conditions, the first term on the right hand side of Eq. (B.1c) can be obtained as:

Loading 1:

$$\{\beta_{cl}\}\{\varepsilon\}T=[Q]\{\alpha\}\{\varepsilon\}T=\begin{Bmatrix}Q_{11}\alpha_1+Q_{12}\alpha_2\\ Q_{12}\alpha_1+Q_{22}\alpha_2\\ 0\end{Bmatrix}\cdot\begin{Bmatrix}\zeta\\ 0\\ 0\end{Bmatrix}T=\left(Q_{11}\alpha_1+Q_{12}\alpha_2\right)\zeta T \tag{B.8a}$$

Loading 2:

$$\{\beta_{cl}\}\{\varepsilon\}T=[Q]\{\alpha\}\{\varepsilon\}T=\begin{Bmatrix}Q_{11}\alpha_1+Q_{12}\alpha_2\\ Q_{12}\alpha_1+Q_{22}\alpha_2\\ 0\end{Bmatrix}\cdot\begin{Bmatrix}0\\ \zeta\\ 0\end{Bmatrix}T=\left(Q_{12}\alpha_1+Q_{22}\alpha_2\right)\zeta T \tag{B.8b}$$

According to PD theory:

Corresponding PD representation can be defined as:

$$\underline{\mathbf{B}}\bullet\underline{\mathbf{U}}T=T\int_H\beta\left(\frac{\mathbf{y}'-\mathbf{y}}{|\mathbf{y}'-\mathbf{y}|}\right)\cdot\mathbf{u}\left(\mathbf{x}'-\mathbf{x}\right)\mathrm{d}H \tag{B.9}$$

By using small angle approximation Eq. (B.9) becomes as (See Fig. B.1):

$$\underline{\mathbf{B}}\bullet\underline{\mathbf{U}}T=T\int_H\beta\eta_X\mathrm{d}H=T\int_H\beta\left(|\mathbf{y}'-\mathbf{y}|-|\mathbf{x}'-\mathbf{x}|\right)\mathrm{d}H \tag{B.10}$$

with

$$\eta_X=u'_X-u_X=\cos(\varphi)\left(u'_x-u_x\right)+\sin(\varphi)\left(u'_y-u_y\right) \tag{B.11}$$

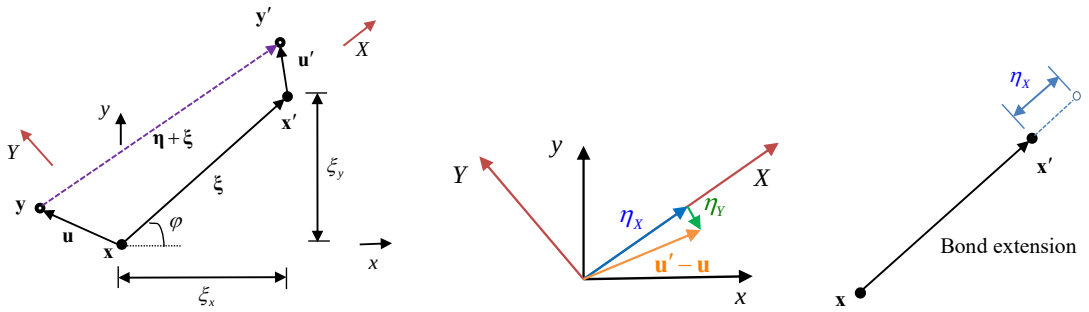

(a) (b) (c)

Fig.B.1 Relative displacement between points $\mathbf{x}$ and $\mathbf{x}'$ in different coordinates [15].

The relative distances in deformed configuration between the material points $\mathbf{x}$ and $\mathbf{x}'$ for given loading conditions are,

Loading 1:

$$|\mathbf{y}'-\mathbf{y}|=\left[1+\zeta\cos^2(\varphi)\right]|\mathbf{x}'-\mathbf{x}| \tag{B.12a}$$

Loading 2:

$$|\mathbf{y}'-\mathbf{y}|=\left[1+\zeta\sin^2(\varphi)\right]|\mathbf{x}'-\mathbf{x}| \tag{B.12b}$$

Eq. (B.10) for given loading conditions can be defined as:

Loading 1:

$$\underline{\mathbf{B}}\cdot\underline{\mathbf{U}}T = T\int_H \left(\mu_f\beta_f + \beta_m\right)\left|\mathbf{x}'-\mathbf{x}\right|\left(\zeta\cos^2\left(\varphi\right)\right)\mathrm{d}H \tag{B.13a}$$

Loading 2:

$$\underline{\mathbf{B}}\cdot\underline{\mathbf{U}}T = T\int_H \left(\mu_f\beta_f + \beta_m\right)\left|\mathbf{x}'-\mathbf{x}\right|\left(\zeta\sin^2\left(\varphi\right)\right)\mathrm{d}H \tag{B.13b}$$

By plugging the relative distances between the material points $\mathbf{x}$ and $\mathbf{x}'$ into Eq.(B.13), Eq.(B.10) becomes

Loading 1:

$$\begin{aligned}\underline{\mathbf{B}}\cdot\underline{\mathbf{U}}T &= T\int_H \left(\mu_f\beta_f + \beta_m\right)\zeta\cos^2\left(\varphi\right)\left|\boldsymbol{\xi}\right|\mathrm{d}H \\ &= T\int_0^{2\pi}\int_0^{\delta}\left(\mu_f\beta_f + \beta_m\right)\zeta\cos^2\left(\varphi\right)\left|\boldsymbol{\xi}\right|h\left|\boldsymbol{\xi}\right|d\left|\boldsymbol{\xi}\right|d\varphi \\ &= \zeta T\left[\sum_{\mathbf{x}'=1}^{N_F}\beta_f\left|\boldsymbol{\xi}\right|V' + \frac{\pi h\delta^3}{3}\beta_m\right]\end{aligned} \tag{B.14a}$$

Loading 2:

$$\begin{aligned}\underline{\mathbf{B}}\cdot\underline{\mathbf{U}}T &= T\int_H \left(\mu_f\beta_f + \beta_m\right)\zeta\sin^2\left(\varphi\right)\left|\boldsymbol{\xi}\right|\mathrm{d}H \\ &= T\int_0^{2\pi}\int_0^{\delta}\left(\mu_f\beta_f + \beta_m\right)\zeta\sin^2\left(\varphi\right)\left|\boldsymbol{\xi}\right|h\left|\boldsymbol{\xi}\right|d\left|\boldsymbol{\xi}\right|d\varphi \\ &= \zeta T\left(\frac{\pi h\delta^3}{3}\beta_m\right)\end{aligned} \tag{B.14b}$$

By equating the expressions (B.14) and (B.8), the follows are obtained as

$$\sum_{\mathbf{x}'=1}^{N_f}\beta_f\left|\boldsymbol{\xi}\right|V' + \frac{\pi h\delta^3}{3}\beta_m = Q_{11}\alpha_1 + Q_{12}\alpha_2 \tag{B.15a}$$

and

$$\frac{\pi h\delta^3}{3}\beta_m = Q_{12}\alpha_1 + Q_{22}\alpha_2 \tag{B.15b}$$

Finally, the expressions of β_f and β_m are defined as

$$\beta_f = \frac{\left(Q_{11}\alpha_1 + Q_{12}\alpha_2\right) - \left(Q_{12}\alpha_1 + Q_{22}\alpha_2\right)}{\sum_{\mathbf{x}'=1}^{N_f}\left|\boldsymbol{\xi}\right|V'} \tag{B.16a}$$

and

$$\beta_m = \frac{3\left(Q_{12}\alpha_1 + Q_{22}\alpha_2\right)}{\pi h\delta^3} \tag{B.16b}$$

PD thermal modulus for a 2-D isotropic material Eq. (B.16) becomes

$$\beta_f = 0 \tag{B.17a}$$

$$\beta_m = \frac{6K\alpha}{\pi h\delta^3} = \frac{3E\alpha}{\pi h\delta^3\left(1-\nu\right)} = \frac{3\beta_{cl}}{\pi h\delta^3} \tag{B.17b}$$

with

$$\alpha_1 = \alpha_2 = \alpha,\ Q_{11} = Q_{22} = K + \mu,\quad Q_{12} = K - \mu \tag{B.18}$$

where K and μ are bulk modulus and Lamé constant, respectively. The PD parameters provided in Eq. (B.17) are consistent with the ones in [25].

Furthermore, for bond based peridynamic theory the PD thermal modulus will reduce to [24];

$$\beta_f = 0 \tag{B.19a}$$

$$\beta_m = \frac{1}{2} c\alpha \tag{B.19b}$$

with

$$c = \frac{9E}{\pi h \delta^3} \text{ for 2-D} \tag{B.19c}$$

B.3 PD thermal modulus expression for multi-layer/ laminate model

In a multi-layer/laminate model, the expressions of the PD thermal modulus associated with in plane bonds remain same with the ones in lamina model (Appendix B.2). The PD thermal model for multi-layer composites including coupling effects can be written as

$$\begin{aligned}\rho c_v \dot{T}_k^n = &\sum_{j=1}^{N_{ply}} \left[\left(\mu_f \kappa_f + \kappa_m\right) \frac{\Theta\left(\mathbf{x}_j^n, t\right) - \Theta\left(\mathbf{x}_k^n, t\right)}{\left|\mathbf{x}_j^n - \mathbf{x}_k^n\right|} - \Theta_0 \left(\mu_f \beta_f + \beta_m\right) \dot{e}_{kj}^n \right] V_j^n \\ &+ \sum_{m=n+1,n-1} \sum_{j=1}^{N_{inter}} \left[\kappa_{inter} \frac{\Theta\left(\mathbf{x}_j^m, t\right) - \Theta\left(\mathbf{x}_k^n, t\right)}{\left|\mathbf{x}_j^m - \mathbf{x}_k^n\right|} - \Theta_0 \beta_{inter} \dot{e}_{kj,z}^{nm} \right] V_j^m + \rho q_b\left(\mathbf{x}_k^n, t\right)\end{aligned} \tag{B.20}$$

Similarly, PD thermal modulus can be found by equating the free energy densities from PD theory and CCM as given in Eq. (B.4) for simple loading conditions.

In order to derive the expression of PD thermal modulus, a uniform transverse normal stretch is applied as

$$\varepsilon_{33} = \zeta \tag{B.21}$$

According to CCM:

Under the given loading condition, the first term on the right hand side of Eq. (B.1c) can be obtained as:

$$\{\beta_{cl}\}\{\varepsilon\} T = \{E_m \alpha_m\}\{\zeta\} T = E_m \alpha_m \zeta T \tag{B.22}$$

According to PD theory:

Under the given loading condition, as illustrated in Fig.B.2, for the material point $\mathbf{x}_k^n$ of interest, the relative positions in undeform and deformed configurations are

$$\left|\mathbf{x}_j^m-\mathbf{x}_k^n\right|=\sqrt{h^2+l^2} \tag{B.23a}$$

$$\left|\mathbf{y}_j^m-\mathbf{y}_k^n\right|=\sqrt{(1+\zeta)^2 h^2+l^2} \tag{B.23b}$$

with $l=\left|\mathbf{y}_j^m-\mathbf{y}_k^m\right|$ and $m=(n+1,n-1)$

Consequently, the relative displacement becomes

$$\left|\mathbf{y}_j^m-\mathbf{y}_k^n\right|-\left|\mathbf{x}_j^m-\mathbf{x}_k^n\right|=\sqrt{(1+\zeta)^2 h^2+l^2}-\sqrt{h^2+l^2}\approx\frac{\zeta h^2}{\sqrt{h^2+l^2}} \tag{B.24}$$

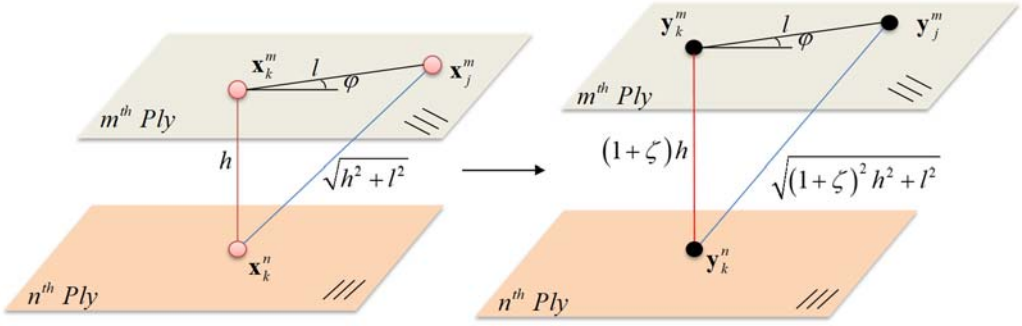

Fig.B.2. Illustration of relative positions in undeform and deformed configurations.

The integration domain, H, is a circle disk with radius being δ and thickness being h. Therefore, by considering the two adjacent plies $(m=n+1,n-1)$, Eq. (B.10) can be calculated as

$$\underline{\mathbf{B}}\bullet\underline{\mathbf{U}}T=2\int_H\beta_{inter}\frac{\zeta h^2}{\sqrt{h^2+l^2}}\mathrm{d}H=2\int_0^{2\pi}\int_0^{\delta}\beta_{inter}\frac{\zeta h^2}{\sqrt{h^2+l^2}}hl\,\mathrm{d}l\,\mathrm{d}\varphi=4\pi\beta_{inter}\zeta h^3\left(\tilde{\delta}-h\right) \tag{B.25}$$

By equating Eq.(B.25) and Eq.(B.22), the expression of β_{inter} can be obtained as

$$\beta_{inter}=\frac{E_m\alpha_m}{4\pi h^3\left(\tilde{\delta}-h\right)} \tag{B.26}$$

Appendix C

The values of the PD parameters depend on the domain of integration which is decided by the horizon. Therefore, surface correction factors are needed when the material points are located near the free surface. The surface correction factors for mechanical parameters for composite materials and isotropic materials have already been provided in [28, 30, 55]. The surface correction factors for PD micro conductivity κ and PD thermal modulus β will be discussed in here.

The surface correction factors of the PD micro conductivity are achieved by comparing the thermal potential obtained from PD and classical formulations under simple loading conditions [23, 28]. The

correctors of thermal modulus can be obtained by equating the free energy densities calculated from the two theories.

C.1 Surface correction factors for PD micro conductivity

Surface correction factors for single layer/lamina model

As illustrated in Fig.C.1, the coordinates of the material point $\mathbf{x}_k$ are denoted as $\left(x_k, y_k\right)$ for global coordinate system and $\left(X_k^1, X_k^2\right)$ for the material coordinate system.

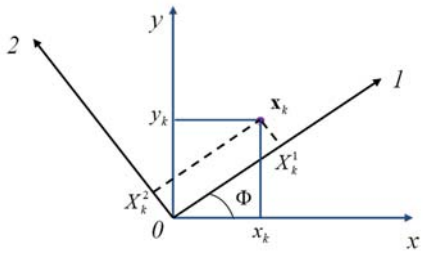

Fig.C.1. Coordinate system illustrations.

A simple linear temperature field, $\Theta = X^1 + X^2$, is applied on the lamina. Corresponding temperature difference between two material points is

$$\Theta_j - \Theta_k = \left(X_j^1 + X_j^2\right) - \left(X_k^1 + X_k^2\right) \tag{C.1}$$

The PD thermal potential at material point $\mathbf{x}_k$ can be expressed as

$$Z_k^{PD} = Z_{k,F}^{PD} + Z_{k,M}^{PD} \tag{C.2}$$

where $Z_{k,F}^{PD}$ and $Z_{k,M}^{PD}$ represent the contributions from fibre thermal bonds and the matrix thermal bonds. By using the expression given in Eq. (A.5), the PD thermal potential can also be expressed as [23, 24]

$$Z_{k,F}^{PD} = \frac{1}{2}\sum_{j=1}^{N_f} \kappa_f \frac{\left(\left(X_j^1 + X_j^2\right) - \left(X_k^1 + X_k^2\right)\right)^2}{2\left|\mathbf{x}_j - \mathbf{x}_k\right|} \tag{C.3a}$$

and

$$Z_{k,M}^{PD}\left(\mathbf{x}_k\right) = \frac{1}{2}\sum_{j=1}^{N_{ply}} \kappa_m \frac{\left(\left(X_j^1 + X_j^2\right) - \left(X_k^1 + X_k^2\right)\right)^2}{2\left|\mathbf{x}_j - \mathbf{x}_k\right|} \tag{C.3b}$$

On the other hand, corresponding thermal potential can be calculated as [23, 28, 30]

$$Z = \frac{1}{2}\left(k_1\left(\frac{\partial\Theta}{\partial X_1}\right)^2 + k_2\left(\frac{\partial\Theta}{\partial X_2}\right)^2\right) = \frac{1}{2}\left(k_1 + k_2\right) \tag{C.4}$$

The lamina will become a matrix material when $k_1 = k_2$, then corresponding thermal potential is

$$Z_M = \frac{1}{2}\left(k_2 \left(\frac{\partial \Theta}{\partial X_1} \right)^2 + k_2 \left(\frac{\partial \Theta}{\partial X_2} \right)^2 \right) = k_2 \tag{C.5}$$

Therefore, the thermal potential given in Eq.(C.5) can be expressed as

$$Z = Z_M + Z_F \tag{C.6}$$

with

$$Z_F = \frac{1}{2}\left(k_1 - k_2\right) \tag{C.7a}$$

and

$$Z_M = k_2 \tag{C.7b}$$

where Z_F and Z_M are the thermal potentials related with the fibre material and matrix material, respectively.

Consequently, the surface correction factors of κ_f and κ_m at point $\mathbf{x}_k$ can be calculated as

$$S_F\left(\mathbf{x}_k\right) = \frac{Z_F}{Z_{k,F}^{PD}} = \frac{\frac{1}{2}\left(k_1 - k_2\right)}{\frac{1}{2}\sum_{j=1}^{N_f} \kappa_f \frac{\left(\left(X_j^1 + X_j^2\right) - \left(X_k^1 + X_k^2\right)\right)^2}{2\left|\mathbf{x}_j - \mathbf{x}_k\right|}} \tag{C.8a}$$

and

$$S_M\left(\mathbf{x}_k\right) = \frac{Z_M}{Z_{k,M}^{PD}} = \frac{k_2}{\frac{1}{2}\sum_{j=1}^{N_{ply}} \kappa_m \frac{\left(\left(X_j^1 + X_j^2\right) - \left(X_k^1 + X_k^2\right)\right)^2}{2\left|\mathbf{x}_j - \mathbf{x}_k\right|}} \tag{C.8b}$$

Surface correction factors for multi-layer composite model

For a multi-layer thermal composite model, the surface correction factors for κ_f and κ_m remain same. Thus only the derivation of the surface correction factors for the interlayer micro conductivity κ_{inter} is explained in this section. A linear temperature field $\Theta(x, y, z) = z$ is applied on all the plies with respect to the global coordinate system. Subsequently, the temperature difference is calculated as

$$\Theta_j^m - \Theta_k^n = z_j^m - z_k^n \tag{C.9}$$

where the point $\mathbf{x}_k^n$ is in the n^{th}, and $\mathbf{x}_j^m$ is in the m^{th} ply. Therefore, the temperature difference is zero between $\mathbf{x}_j^n$ and $\mathbf{x}_k^n$. The thermal potential of point $\mathbf{x}_k^n$ can be calculated as

$$Z_{inter}^{PD} = \sum_{m=n+1,n-1} \frac{1}{2}\sum_{j=1}^{N_{inter}} \kappa_{inter} \frac{\left(z_j^m - z_k^n\right)^2}{2\left|\xi\right|} = \begin{cases} \frac{1}{2}\sum_{j=1}^{N_{inter}} \kappa_{inter} \frac{h^2}{2\left|\mathbf{x}_j^m - \mathbf{x}_k^n\right|} & \text{for } n = 1, N \\ \sum_{m=n-1,\, n+1} \frac{1}{2}\sum_{j=1}^{N_{inter}} \kappa_{inter} \frac{h^2}{2\left|\mathbf{x}_j^m - \mathbf{x}_k^n\right|} & \text{for } n = 2, 3, \cdots N-1 \end{cases} \tag{C.10}$$

where N is the total number of plies in a laminate (Fig. 6).

Corresponding thermal potential in CCM can be calculated as

$$Z_{\text{inter}} = \frac{1}{2}\left(k_3 \left(\frac{\partial \Theta}{\partial z} \right)^2 \right) = \frac{1}{2} k_3 \tag{C.11}$$

There is only one adjacent layer for the bottom and top ply. However, the value of κ_{inter} is calculated by summing the thermal potential energy developed by two plies. Therefore, surface correction factors for the points in bottom and top ply, the PD thermal potential developed by interlayer thermal bonds are doubled. In conclusion, the surface correction factors for κ_{inter} are given as

$$S_{inter}\left(\mathbf{x}_k^n\right) = \frac{Z_{inter}}{Z_{inter}^{PD}} = \begin{cases} \dfrac{\frac{1}{2}k_3}{2\left(\frac{1}{2}\sum_{j=1}^{N_{inter}} \kappa_{inter} \dfrac{h^2}{2\left|\mathbf{x}_j^m - \mathbf{x}_k^n\right|}\right)} & \text{for } n = 1,\ N \\ \dfrac{\frac{1}{2}k_3}{\sum_{m=n-1,\ n+1} \frac{1}{2}\sum_{j=1}^{N_{inter}} \kappa_{inter} \dfrac{h^2}{2\left|\mathbf{x}_j^m - \mathbf{x}_k^n\right|}} & \textit{for } n = 2,3,\cdots N-1 \end{cases} \tag{C.12}$$

where h is the thickness of single layer (Fig. 6).

C.2 Surface correction factors for PD thermal modulus

Surface correction factors for single-layer composite model

The surface correction factors for PD thermal moduli β_f and β_m is determined by applying two different loading conditions as in the fibre direction then in transverse direction as:

Loading 1:

$$\mathbf{u}_1 = \{\zeta x_1 \quad 0\} \tag{C.13a}$$

Loading 2:

$$\mathbf{u}_2 = \{0 \quad \zeta x_2\} \tag{C.13b}$$

The orthotropic property of a single layer composite is assumed as the summation of a matrix material and a fibre material that only exists in the fibre direction. In analogy with the PD thermal modulus components, the classical thermal modulus β_{cl} is assumed to be

$$\beta_{cl} = \begin{Bmatrix} \beta_{cl}^f + \beta_{cl}^m \\ \beta_{cl}^m \\ 0 \end{Bmatrix} = \begin{Bmatrix} Q_{11}\alpha_1 + Q_{12}\alpha_2 \\ Q_{12}\alpha_1 + Q_{22}\alpha_2 \\ 0 \end{Bmatrix} \tag{C.14a}$$

with

$$\beta_{cl}^{f} = \left(Q_{11}\alpha_1 + Q_{12}\alpha_2\right) - \left(Q_{12}\alpha_1 + Q_{22}\alpha_2\right) \tag{C.14b}$$

$$\beta_{cl}^{m} = Q_{12}\alpha_1 + Q_{22}\alpha_2 \tag{C.14c}$$

Under given loading conditions, the first term on the right hand side of Eq. (B.1c) can be obtained as:

Load 1:

$$\{\beta_{cl}\}\{\varepsilon\}T = [Q]\{\alpha\}\{\varepsilon\}T = \begin{Bmatrix} Q_{11}\alpha_1 + Q_{12}\alpha_2 \\ Q_{12}\alpha_1 + Q_{22}\alpha_2 \\ 0 \end{Bmatrix} \cdot \begin{Bmatrix} \zeta \\ 0 \\ 0 \end{Bmatrix} T = \left(Q_{11}\alpha_1 + Q_{12}\alpha_2\right)\zeta T \tag{C.15a}$$

with

$$\left\{\beta_{cl}^{f,1}\right\}\{\varepsilon\}T = \left[\left(Q_{11}\alpha_1 + Q_{12}\alpha_2\right) - \left(Q_{12}\alpha_1 + Q_{22}\alpha_2\right)\right]\zeta T \tag{C.15b}$$

$$\left\{\beta_{cl}^{m,1}\right\}\{\varepsilon\}T = \left[Q_{12}\alpha_1 + Q_{22}\alpha_2\right]\zeta T \tag{C.15c}$$

Load 2:

$$\{\beta_{cl}\}\{\varepsilon\}T = [Q]\{\alpha\}\{\varepsilon\}T = \begin{Bmatrix} Q_{11}\alpha_1 + Q_{12}\alpha_2 \\ Q_{12}\alpha_1 + Q_{22}\alpha_2 \\ 0 \end{Bmatrix} \cdot \begin{Bmatrix} 0 \\ \zeta \\ 0 \end{Bmatrix} T = \left(Q_{12}\alpha_1 + Q_{22}\alpha_2\right)\zeta T \tag{C.16a}$$

with

$$\left\{\beta_{cl}^{f,2}\right\}\{\varepsilon\}T = 0 \tag{C.16b}$$

$$\left\{\beta_{cl}^{m,2}\right\}\{\varepsilon\}T = \left[Q_{12}\alpha_1 + Q_{22}\alpha_2\right]\zeta T \tag{C.16c}$$

Since there is no deformation in the fibre direction, the fibres do not deform under load 2. Therefore, the deformation effect of fibre on temperature is zero.

Corresponding PD representation can be defined by using Eq. (B.9) as:

Load 1:

$$\left(\underline{\mathbf{B}} \bullet \underline{\mathbf{U}}\right)^{f,1} T = T\sum_{j=1}^{N_f} \beta_f \left(\mathbf{u}_1\left(\mathbf{x}_j\right) - \mathbf{u}_1\left(\mathbf{x}_k\right)\right) \cdot \frac{\mathbf{y}_j - \mathbf{y}_k}{\left|\mathbf{y}_j - \mathbf{y}_k\right|} V_j \tag{C.17a}$$

$$\left(\underline{\mathbf{B}} \bullet \underline{\mathbf{U}}\right)^{m,1} T = T\sum_{j=1}^{N_{ply}} \beta_m \left(\mathbf{u}_1\left(\mathbf{x}_j\right) - \mathbf{u}_1\left(\mathbf{x}_k\right)\right) \cdot \frac{\mathbf{y}_j - \mathbf{y}_k}{\left|\mathbf{y}_j - \mathbf{y}_k\right|} V_j \tag{C.17b}$$

Load 2:

$$\left(\underline{\mathbf{B}} \bullet \underline{\mathbf{U}}\right)^{f,2} T = 0 \tag{C.18a}$$

$$\left(\underline{\mathbf{B}} \bullet \underline{\mathbf{U}}\right)^{m,2} T = T\sum_{j=1}^{N_{ply}} \beta_m \left(\mathbf{u}_2\left(\mathbf{x}_j\right) - \mathbf{u}_2\left(\mathbf{x}_k\right)\right) \cdot \frac{\mathbf{y}_j - \mathbf{y}_k}{\left|\mathbf{y}_j - \mathbf{y}_k\right|} V_j \tag{C.18b}$$

As a result, the surface correction factors are

$$S_F^1\left(\mathbf{x}_k,\mathbf{x}_j\right)=\frac{\left\{\beta_{cl}^{f,1}\right\}\{\varepsilon\}T}{\left(\underline{\mathbf{B}}\bullet\underline{\mathbf{U}}\right)^{f,1}T}=\frac{\left[\left(Q_{11}\alpha_1+Q_{12}\alpha_2\right)-\left(Q_{12}\alpha_1+Q_{22}\alpha_2\right)\right]\zeta}{\sum_{j=1}^{N_f}\beta_f\left(\mathbf{u}_1\left(\mathbf{x}_j\right)-\mathbf{u}_1\left(\mathbf{x}_k\right)\right)\cdot\frac{\mathbf{y}_j-\mathbf{y}_k}{\left|\mathbf{y}_j-\mathbf{y}_k\right|}V_j} \tag{C.19a}$$

$$S_M^1\left(\mathbf{x}_k,\mathbf{x}_j\right)=\frac{\left\{\beta_{cl}^{m,1}\right\}\{\varepsilon\}T}{\left(\underline{\mathbf{B}}\bullet\underline{\mathbf{U}}\right)^{m,1}T}=\frac{\left[Q_{12}\alpha_1+Q_{22}\alpha_2\right]\zeta}{\sum_{j=1}^{N_{ply}}\beta_m\left(\mathbf{u}_1\left(\mathbf{x}_j\right)-\mathbf{u}_1\left(\mathbf{x}_k\right)\right)\cdot\frac{\mathbf{y}_j-\mathbf{y}_k}{\left|\mathbf{y}_j-\mathbf{y}_k\right|}V_j} \tag{C.19b}$$

$$S_F^2\left(\mathbf{x}_k,\mathbf{x}_j\right)=1 \tag{C.19c}$$

$$S_M^2\left(\mathbf{x}_k,\mathbf{x}_j\right)=\frac{\left\{\beta_{cl}^{m,2}\right\}\{\varepsilon\}T}{\left(\underline{\mathbf{B}}\bullet\underline{\mathbf{U}}\right)^{m,2}T}=\frac{\left[Q_{12}\alpha_1+Q_{22}\alpha_2\right]\zeta}{\sum_{j=1}^{N_{ply}}\beta_m\left(\mathbf{u}_2\left(\mathbf{x}_j\right)-\mathbf{u}_2\left(\mathbf{x}_k\right)\right)\cdot\frac{\mathbf{y}_j-\mathbf{y}_k}{\left|\mathbf{y}_j-\mathbf{y}_k\right|}V_j} \tag{C.19d}$$

It should be noted that these correction factors are validated for the fibre and transverse directions. They can act as the principal values of an ellipse [30] to approximate the surface corrections in any other directions as

$$S_F\left(\mathbf{x}_k,\mathbf{x}_j\right)=1/\sqrt{\left(n_1/S_F^1\left(\mathbf{x}_k,\mathbf{x}_j\right)\right)^2+\left(n_2/S_F^2\left(\mathbf{x}_k,\mathbf{x}_j\right)\right)^2} \tag{C.20a}$$

and

$$S_M\left(\mathbf{x}_k,\mathbf{x}_j\right)=1/\sqrt{\left(n_1/S_M^1\left(\mathbf{x}_k\right)\right)^2+\left(n_2/S_M^2\left(\mathbf{x}_k\right)\right)^2}\,, \tag{C.20b}$$

where n_1 and n_2 are the projections of the relative position vector between $\mathbf{x}_k$ and $\mathbf{x}_j$ on fibre and transverse directions.

Surface correction factors for multi-layer composite model

For a multi-layer composite model, the surface correction factors for in-plane directions remain the same with the ones calculated in lamina model. The surface correction factor for the thickness direction is developed. A third loading condition is applied as

Load 3:

$$\mathbf{u}_3=\left\{0\quad 0\quad \zeta z\right\} \tag{C.21}$$

Under given loading condition, the second term on the right hand side in Eq. (B.1c) can be obtained as:

$$\left\{\beta_{cl}\right\}\{\varepsilon\}T=E_m\alpha_m\zeta T \tag{C.22}$$

Corresponding PD representation can be defined by using Eq. (B.9) as

$$\underline{\mathbf{B}}\bullet\underline{\mathbf{U}}T=T\sum_{m=n+1,n-1}\sum_{j=1}^{N_{inter}}\beta_{inter}\left(\mathbf{u}_z\left(\mathbf{x}_j\right)-\mathbf{u}_z\left(\mathbf{x}_k\right)\right)\cdot\frac{\mathbf{y}_j-\mathbf{y}_k}{\left|\mathbf{y}_j-\mathbf{y}_k\right|}V_j^m \tag{C.23}$$

Then the surface correction factor for β_{inter} is

$$S_z^{\beta}\left(\mathbf{x}_k^n,\mathbf{x}_j^m\right)=\frac{\{\beta_{cl}\}\{\varepsilon\}T}{\underline{\mathbf{B}}\bullet\underline{\mathbf{U}}T}=\begin{cases}\dfrac{E_m\alpha_m\zeta}{2\sum\limits_{j=1}^{N_{inter}}\beta_{inter}\left(\mathbf{u}_z\left(\mathbf{x}_j\right)-\mathbf{u}_z\left(\mathbf{x}_k\right)\right)\cdot\dfrac{\mathbf{y}_j-\mathbf{y}_k}{\left|\mathbf{y}_j-\mathbf{y}_k\right|}V_j^m} & \text{for } n=1,N\\ \dfrac{E_m\alpha_m\zeta}{\sum\limits_{m=n+1,n-1}\sum\limits_{j=1}^{N_{inter}}\beta_{inter}\left(\mathbf{u}_z\left(\mathbf{x}_j\right)-\mathbf{u}_z\left(\mathbf{x}_k\right)\right)\cdot\dfrac{\mathbf{y}_j-\mathbf{y}_k}{\left|\mathbf{y}_j-\mathbf{y}_k\right|}V_j^m} & n=2,3,\cdots N-1\end{cases} \tag{C.24}$$

References

[1] Prewo KM, Brennan JJ. High-Strength Silicon-Carbide Fiber-Reinforced Glass-Matrix Composites. J Mater Sci. 1980;15:463-8.

[2] Carter JP, Booker JR. Finite-Element Analysis of Coupled Thermoelasticity. Comput Struct. 1989;31:73-80.

[3] Biot MA. Thermoelasticity and Irreversible Thermodynamics. J Appl Phys. 1956;27:240-53.

[4] Hetnarski RB, Ignaczak J. Generalized thermoelasticity. J Therm Stresses. 1999;22:451-76.

[5] Dillon O, Tauchert T. The experimental technique for observing the temperatures due to the coupled thermoelastic effect. Int J Solids Struct. 1966;2:385IN1389-388IN4391.

[6] Zenkour AM. Three-dimensional thermal shock plate problem within the framework of different thermoelasticity theories. Compos Struct. 2015;132:1029-42.

[7] Stanley P. Applications and potential of thermoelastic stress analysis. J Mater Process Tech. 1997;64:359-70.

[8] Ene HI. On Linear Thermoelasticity of Composite-Materials. Int J Eng Sci. 1983;21:443-8.

[9] Rao DM, Sinha PK. Finite element coupled thermostructural analysis of composite beams. Comput Struct. 1997;63:539-49.

[10] Mukherjee N, Sinha PK. Thermal shocks in composite plates: A coupled thermoelastic finite element analysis. Compos Struct. 1996;34:1-12.

[11] Khan KA, Barello R, Muliana AH, Levesque M. Coupled heat conduction and thermal stress analyses in particulate composites. Mech Mater. 2011;43:608-25.

[12] Kogl M, Gaul L. A boundary element method for anisotropic coupled thermoelasticity. Arch Appl Mech. 2003;73:377-98.

[13] Brischetto S, Carrera E. Coupled thermo-mechanical analysis of one-layered and multilayered plates. Compos Struct. 2010;92:1793-812.

[14] Silling SA. Reformulation of elasticity theory for discontinuities and long-range forces. J Mech Phys Solids. 2000;48:175-209.

[15] Oterkus E, Madenci E. Peridynamic Analysis of Fiber-Reinforced Composite Materials. J Mech Mater Struct. 2012;7:45-84.

[16] Oterkus E, Madenci E, Weckner O, Silling S, Bogert P, Tessler A. Combined finite element and peridynamic analyses for predicting failure in a stiffened composite curved panel with a central slot. Compos Struct. 2012;94:839-50.

[17] Oterkus E, Madenci E. Peridynamic Theory for Damage Initiation and Growth in Composite Laminate. Key Eng Mater. 2012;488-489:355-8.

[18] Kilic B, Agwai A, Madenci E. Peridynamic theory for progressive damage prediction in center-cracked composite laminates. Compos Struct. 2009;90:141-51.

[19] Oterkus E. Peridynamic theory for modeling three-dimensional damage growth in metallic and composite structures [Doctor of philosophy]. Arizona: University of Arizona, 2010.

[20] Silling SA, Epton M, Weckner O, Xu J, Askari E. Peridynamic states and constitutive modeling. J Elasticity. 2007;88:151-84.

[21] Oterkus S, Madenci E. Fully coupled thermomechanical analysis of fiber reinforced composites using peridynamics. 55th AIAA/ASMe/ASCE/AHS/SC Structures, Structural Dynamics, and Materials Conference-SciTech Forum and Exposition. Maryland2014.

[22] Gao Y, Oterkus S. Peridynamic Analysis of Marine Composites under Shock Loads by Considering Thermomechanical Coupling Effects. Journal of Marine Science and Engineering. 2018;6:38.

[23] Oterkus S, Madenci E, Agwai A. Peridynamic thermal diffusion. J Comput Phys. 2014;265:71-96.
[24] Oterkus S, Madenci E, Agwai A. Fully coupled peridynamic thermomechanics. J Mech Phys Solids. 2014;64:1-23.
[25] Gao Y, Oterkus S. Ordinary state-based peridynamic modelling for fully coupled thermoelastic problems. Continuum Mech Therm. 2018.
[26] Askari A, Azdoud Y, Han F, Lubineau G, Silling S. Peridynamics for analysis of failure in advanced composite materials. 2014.
[27] Agwai AG. A Peridynamic Approach for Coupled Fields [Doctor of philosophy]. Arizona: The University of Arizona., 2011.
[28] Oterkus S. Peridynamics for the solution of multiphysics problems [Doctor of Philosophy]. Arizona: The University of Arizona, 2015.
[29] Madenci E, Oterkus S. Peridynamics for Coupled Field Equations. Handbook of Peridynamic Modeling. New York: Chapman and Hall/CRC; 2016. p. 490-528.
[30] Madenci E, Oterkus E. Peridynamic theory and its applications: Springer, 2014.
[31] Colavito KW. Peridynamics for Failure and Residual Strength Prediction of Fiber-Reinforced Composites [Doctor of Philosophy]. Arizona: The University of Arizona., 2013.
[32] Oterkus E, Madenci E. Peridynamics for Failure Prediction in Composites. 53rd AIAA/ASME/ASCE/AHS/ASC Structures, Structural Dynamics and Materials Conference: American Institute of Aeronautics and Astronautics; 2012.
[33] Nettles A. Basic mechanics of laminated composite plates. National Aeronautics and Space Administration, Huntsville, AL (United States). George C. Marshall Space Flight Center; 1994.
[34] Kaw AK. Mechanics of composite materials: CRC press, 2005.
[35] Vazic B, Wang H, Diyaroglu C, Oterkus S, Oterkus E. Dynamic propagation of a macrocrack interacting with parallel small cracks. Aims Materials Science. 2017;4:118-36.
[36] Ayatollahi M, Aliha M. Analysis of a new specimen for mixed mode fracture tests on brittle materials. Eng Fract Mech. 2009;76:1563-73.
[37] Diyaroglu C, Oterkus E, Madenci E, Rabczuk T, Siddiq A. Peridynamic modeling of composite laminates under explosive loading. Compos Struct. 2016;144:14-23.
[38] Oterkus S, Madenci E. Peridynamic modeling of fuel pellet cracking. Eng Fract Mech. 2017;176:23-37.
[39] Silling SA, Askari E. A meshfree method based on the peridynamic model of solid mechanics. Comput Struct. 2005;83:1526-35.
[40] Kilic B, Madenci E. An adaptive dynamic relaxation method for quasi-static simulations using the peridynamic theory. Theor Appl Fract Mec. 2010;53:194-204.
[41] Berthelot J-M. Classical Laminate Theory. In: Berthelot J-M, editor. Composite Materials: Mechanical Behavior and Structural Analysis. New York, NY: Springer New York; 1999. p. 287-311.
[42] Staab G. Laminar composites. Woburn: Butterworth-Heinemann, 2015.
[43] Le Q, Bobaru F. Surface corrections for peridynamic models in elasticity and fracture. Comput Mech. 2017:1-20.
[44] Madenci E, Guven I. The finite element method and applications in engineering using ANSYS®. US: Springer, 2015.
[45] Hetnarski RB, Eslami MR, Gladwell G. Thermal stresses: advanced theory and applications: Springer, 2009.
[46] King J. Failure in composite materials. Metals and Materials. 1989;5:720-6.
[47] Bogert P, Satyanarayana A, Chunchu P. Comparison of Damage Path Predictions for Composite Laminates by Explicit and Standard Finite Element Analysis Tools. 47th AIAA/ASME/ASCE/AHS/ASC Structures, Structural Dynamics, and Materials Conference: American Institute of Aeronautics and Astronautics; 2006.
[48] Alpay S, Madenci E. Crack Growth Prediction in Fully-Coupled Thermal and Deformation Fields Using Peridynamic Theory. 54th AIAA/ASME/ASCE/AHS/ASC Structures, Structural Dynamics, and Materials Conference2013. p. 1477.
[49] Wu EM, Reuter Jr R. Crack extension in fiberglass reinforced plastics. University of Illinois; 1965.
[50] Jose S, Ramesh Kumar R, Jana MK, Venkateswara Rao G. Intralaminar fracture toughness of a cross-ply laminate and its constituent sub-laminates. Compos Sci Technol. 2001;61:1115-22.

[51] Li X, Hallett SR, Wisnom MR, Zobeiry N, Vaziri R, Poursartip A. Experimental study of damage propagation in Over-height Compact Tension tests. Composites Part A: Applied Science and Manufacturing. 2009;40:1891-9.
[52] Manders PW, Chou T-W, Jones FR, Rock JW. Statistical analysis of multiple fracture in 0°/90°/0° glass fibre/epoxy resin laminates. J Mater Sci. 1983;18:2876-89.
[53] Nowinski JL. Theory of thermoelasticity with applications: Sijthoff & Noordhoff International Publishers, 1978.
[54] Silling SA. Linearized Theory of Peridynamic States. J Elasticity. 2010;99:85-111.
[55] Madenci E, Oterkus S. Ordinary state-based peridynamics for plastic deformation according to von Mises yield criteria with isotropic hardening. J Mech Phys Solids. 2016;86:192-219.
[56] Madenci E, Oterkus S. Ordinary state-based peridynamics for thermoviscoelastic deformation. Eng Fract Mech. 2017;175:31-45.